

1 Implementing a dynamic representation of fire and harvest including 2 subgrid-scale heterogeneity in the tile-based land surface model 3 CLASSIC v1.45

4 Salvatore R. Curasi^{1,2,<https://orcid.org/0000-0002-4534-3344>}, Joe R. Melton^{1,<https://orcid.org/0000-0002-9414-064X>}, Elyn R.
5 Humphreys^{2,<https://orcid.org/0000-0002-5397-2802>}, Txomin Hermosilla^{3,<https://orcid.org/0000-0002-5445-0360>}, Michael A.
6 Wulder^{3,<https://orcid.org/0000-0002-6942-1896>}

7 ¹Climate Research Division, Environment, and Climate Change Canada, Victoria, BC, V8N 1V8, Canada

8 ²Department of Geography & Environmental Studies, Carleton University, Ottawa, ON, K1S 5B6, Canada

9 ³Canadian Forest Service (Pacific Forestry Centre), Natural Resources Canada, Victoria, BC, V8Z 1M5, Canada

10
11 *Correspondence to:* Salvatore R. Curasi (sal.curasi@ec.gc.ca)

12
13 **Abstract.** Canada’s forests play a critical role in the global carbon (C) cycle and are responding to unprecedented climate
14 change as well as ongoing natural and anthropogenic disturbances. However, the representation of disturbance in boreal regions
15 is limited in pre-existing land surface models (LSMs). Moreover, many LSMs do not explicitly represent subgrid-scale
16 heterogeneity resulting from disturbance. To address these limitations, we implement harvest and wildfire forcings in the
17 Canadian Land Surface Scheme Including Biogeochemical Cycles (CLASSIC) land surface model alongside dynamic tiling
18 that represents subgrid-scale heterogeneity due to disturbance. The disturbances are captured using 30-m spatial resolution
19 satellite data (Landsat) on an annual basis for 33 years. Using the pan-Canadian domain (i.e. all of Canada south of 76°N) as
20 our study area for demonstration, we determine the model setup that optimally balances detailed process representation and
21 computational efficiency. We then demonstrate the impacts of subgrid-scale heterogeneity relative to standard average
22 individual-based representations of disturbance and explore the resultant differences between the simulations. Our results
23 indicate that the modeling approach implemented can balance model complexity and computational cost to represent the
24 impacts of subgrid-scale heterogeneity resulting from disturbance. Subgrid-scale heterogeneity is shown to have impacts 1.5
25 to 4 times the impact of disturbance alone on gross primary productivity, autotrophic respiration, and surface energy balance
26 processes in our simulations. These impacts are a result of subgrid-scale heterogeneity slowing vegetation re-growth and
27 affecting surface energy balance in recently disturbed, sparsely vegetated, and often snow-covered fractions of the land surface.
28 Representing subgrid-scale heterogeneity is key to more accurately representing timber harvest, which preferentially impacts
29 larger trees on higher quality and more accessible sites. Our results show how different discretization schemes can impact
30 model biases resulting from the representation of disturbance. These insights, along with our implementation of dynamic tiling

31 may apply to other tile-based LSMs. Ultimately our results enhance our understanding of, and ability to, represent disturbance
32 within Canada to facilitate a comprehensive process-based assessment of Canada's terrestrial C cycle.

33

34 **Copyright statement**

35 The works published in this journal are distributed under the Creative Commons Attribution 4.0 License. This license does not
36 affect the Crown copyright work, which is reusable under the Open Government Licence (OGL). The Creative Commons
37 Attribution 4.0 License and the OGL are interoperable and do not conflict with, reduce, or limit each other.

38 ©Crown copyright 2023

39 **1 Introduction**

40 Canada's forests play a critical role in the global carbon (C) cycle (Keenan and Williams, 2018; Lenton et al., 2008). Canada's
41 forests are also responding to both unprecedented climate change and on-going anthropogenic disturbance (Lenton et al., 2008;
42 White et al., 2017). Unfortunately, disentangling the relative impacts of disturbance processes and climate change on the
43 Canadian forest C cycle is difficult (Sulla-Menashe et al., 2018; Goetz et al., 2005; Ju and Masek, 2016; Weber and Flannigan,
44 1997). Process-based land surface models (LSMs) provide a tool to evaluate the impacts of both types of disturbance but there
45 has only been limited representation of anthropogenic disturbance in regional or global C cycling assessments (Friedlingstein
46 et al., 2019; Peng et al., 2014; Chaste et al., 2017; Hayes et al., 2012). Moreover, of those LSMs that do explicitly represent
47 anthropogenic disturbance, only a small subset account for the resulting subgrid-scale heterogeneity (Le Quéré et al., 2018;
48 Nabel et al., 2020; Pongratz et al., 2018). Here we demonstrate the impacts of disturbance and sub-grid scale heterogeneity on
49 C and energy fluxes, by implementing a dynamic tiling scheme in the Canadian Land Surface Scheme Including
50 Biogeochemical Cycles (CLASSIC).

51

52 Subgrid-scale landscape heterogeneity refers to any characteristic of the landscape that differs at scales below that of the main
53 model grid, in this case, differences in tree age and biomass in burned or harvested subfraction of the grid cell. Tile-based
54 LSMs, unlike individual-based models (i.e. models which simulate the landscape using several heterogeneous individuals), do
55 not inherently represent subgrid-scale heterogeneity. Instead, the tile represents the average individual of a given plant function
56 type (PFT) and thus represents the PFT's average state within the grid cell (e.g. a single height, biomass, etc.), which is used
57 to simulate fluxes. Although most tile-based LSMs account for wood harvest, few represent the resulting subgrid-scale
58 landscape heterogeneity and rather represent disturbances impact on the average individual PFT (Le Quéré et al., 2018;
59 Pongratz et al., 2018; Nabel et al., 2020).

60

61 Stand-replacing forest disturbances (i.e. timber harvest and fire) directly impact forest C stocks through the removal of standing
62 biomass (Wulder et al., 2020). In addition, stand-replacing disturbances also impact stand structure, especially in the case of

63 managed timber harvest (Pan et al., 2010; Kuuluvainen and Gauthier, 2018; Pan et al., 2013). The resulting stand structure
64 impacts forest function such as the the exchange of matter and energy with the atmosphere as well as forest response to climate
65 change (Erb et al., 2017; Luysaert et al., 2014; Körner, 2006; Dore et al., 2010; Liu, 2005; Maness et al., 2012; Hirano et al.,
66 2017). Historically 0.4% of Canada's ~650 Mh of forested ecosystems are affected by stand-replacing disturbance per year
67 (White et al., 2017). The age structure of Canadian forests due to historical disturbance has impacted the strength of the
68 historical C sink in Canadian forests (Kurz and Apps, 1999, 1993; Böttcher et al., 2008). Age structure resulting from
69 disturbance also influences the surface energy balance of stands for example by altering sensible heat flux due to differences
70 in snow cover and albedo and altering the seasonality of surface energy budgets and land surface properties (Liu, 2005; Maness
71 et al., 2012). Therefore, it is key that we enhance our ability to accurately represent both disturbance processes and the influence
72 of subgrid-scale heterogeneity that disturbances produce within LSMs.

73

74 Disturbance events impact the response of Canada's forests to climate change. The response of forest productivity, forest soil
75 decomposition processes, and evaporation rates to warming, rising CO₂ concentrations, and changes to precipitation regimes
76 will depend on stand structural characteristics and tree species characteristics (Hember et al., 2012; Kurz et al., 1997; Körner,
77 2006; Shrestha and Chen, 2010; Bond-Lamberty and Gower, 2008; Czimczik et al., 2006; Kurz et al., 2008). Warmer
78 temperatures and higher atmospheric CO₂ concentrations are likely to increase the productivity of boreal forests, whereas
79 drought stress and changing disturbance regimes are likely to decrease productivity and enhance the decomposition of soil C
80 leading to a patchwork of contrasting future responses (Babst et al., 2019; Reich et al., 2018; Lenton et al., 2008; Weber and
81 Flannigan, 1997; Potapov et al., 2008; Ju and Chen, 2008; Sulla-Menashe et al., 2018). Complex changes in vegetation
82 productivity have already been observed across the pan-Canadian domain due to the intermingling of different disturbance
83 regimes and different vegetation sensitivity to climate change (Marchand et al., 2018; D'Orangeville et al., 2018; Ma et al.,
84 2012; Girardin et al., 2016). Decreases in vegetation productivity are generally occurring in northwestern boreal forests,
85 whereas southeastern boreal forests show positive trends (Marchand et al., 2018). Much of the landscape scale change in
86 vegetation productivity detected across Canada's boreal forests is a product of or influenced by, stand-replacing disturbance
87 (Hermosilla et al., 2015b, a). Some negative productivity trends in the southern fringes of western undisturbed forests can
88 largely be attributed to moisture stress and some of the positive trends in cooler and wetter portions of eastern boreal forests
89 can be attributed to warming (Marchand et al., 2018; Sulla-Menashe et al., 2018). Process-based models which represent both
90 disturbance and the resultant subgrid-scale landscape heterogeneity can offer insight into the drivers of these complex trends
91 (Böttcher et al., 2008).

92

93 CLASSIC is a tile-based LSM that can be coupled to the Canadian Earth System Model (CanESM). Several methods are
94 available for representing disturbance history in tile-based LSMs. Some models represent the age classes within the stand using
95 a fixed number of tiles to represent fractional areas below the scale of the main model grid (i.e. from 2 to 12 tiles) (Shevliakova
96 et al., 2009; Yue et al., 2018a; Naudts et al., 2015; Yang et al., 2010; Stocker et al., 2014). Alternatively, several models

97 simulate subgrid scale forest structure using another model housed in a separate module coupled to the main model (Bellassen
98 et al., 2010; Haverd et al., 2014). The module takes information about net primary productivity from the main model and uses
99 it to simulate and track the growth of individual trees. The module then returns grid cell average state information (i.e. biomass
100 and litter fluxes) which is used by the main model to simulate subsequent fluxes. Finally, a recently developed approach uses
101 a fixed number of tiles to represent age classes (Nabel et al., 2020). Tile fractional area and associated state variables (i.e.
102 biomass C) are horizontally exchanged between the tiles to represent processes like aging, harvest, and disturbance. Each
103 approach entails a host of strengths and weaknesses as well as its own biases resulting from discretization error (Nabel et al.,
104 2020; Fisher et al., 2018).

105

106 In this study, to demonstrate the impacts of disturbance and sub-grid scale heterogeneity on C and energy fluxes, we implement
107 a dynamic tiling scheme in CLASSIC. Our implementation is a modified version of approaches that use a fixed number of
108 tiles to represent age classes within the stand and may apply to other tile-based LSMs. We build upon a version of CLASSIC
109 tailored to the pan-Canadian domain using region-specific plant functional types (PFTs) and a 0.22° (~20 km x 20 km) common
110 grid (Curasi et al., 2022). The age classes within the stand are represented using a variable number of sub-grid tiles of variable
111 fractional area and subject to a user-determined maximum number of tiles available for the simulation. Tiles are split to
112 represent disturbance and the resulting age and size structures. Tiles, and their underlying characteristics, are joined by the
113 simulation either when the number of tiles reaches the user-determined maximum bound or pre-emptively based upon other
114 user-determined parameters. The model is driven by externally forced harvest and fire from region-specific disturbance history
115 drivers. We set an optimal maximum number of tiles available for the simulation by evaluating different model setups through
116 model-on-model evaluation and assessing the run time of these setups. Finally, we compare the differences across runs to
117 assess the impacts of the imposed trade-off between run time and a more detailed representation (i.e. more tiles). This
118 investigation provides insight into the model configuration and role of fire, harvest, and tiling within CLASSIC, as a step
119 towards a comprehensive process-based assessment of Canada's terrestrial C cycle. These insights may also apply to other tile
120 base LSMs.

121 **2 Methods**

122 **2.1 Study area**

123 We use all of Canada south of 76°N as our simulation study area. Canada contains 650 Mha of forested land and 98 Mha (18%)
124 of this forested land was disturbed from 1985 - 2015. On average each year 1.61 Mha is disturbed by wildfire, whereas 0.64
125 Mha is disturbed by harvest (Hermosilla et al., 2019). Disturbance due to wildfire is most prevalent in northern boreal regions,
126 whereas harvest and other anthropogenic disturbances are more common in southern boreal regions where wildfire is
127 suppressed. The spatial extent of individual disturbances is highly variable. In Canada, over the course of a year, each
128 contiguous timber harvest event clears on average 98 ± 115 ha. These timber harvest patterns are heavily influenced by forest

129 management practices (Hermosilla et al., 2015b; White et al., 2017). Similarly, over the course of a year, each contiguous fire
130 event burns 324 ± 633 ha (Hermosilla et al., 2015b). The spatial scale of these change objects, sourced from 30-m spatial
131 resolution Landsat imagery, falls well below the $\sim 40,000$ ha resolution of the 0.22° pan-Canadian domain model grid. Located
132 largely in southern latitudes, around 52% of Canada's forested land is considered managed forest (Stinson et al., 2011).
133 Canada's forest structure is characterized by relatively young stands in central and northwestern Canada, with much older
134 stands found in the Pacific coastal and interior forests in British Columbia (Maltman et al., 2023). Forest ages in Canada are
135 the result of prevailing natural disturbance regimes and, to a lesser extent, forest management practices (Pan et al., 2013).

136 **2.2 The CLASSIC model**

137 CLASSIC is an open-source community model that couples the Canadian Land Surface Scheme (CLASS) (Verseghy, 2000,
138 2017; Verseghy et al., 1993; Verseghy, 2007) and the Canadian Terrestrial Ecosystem Model (CTEM) (Melton and Arora,
139 2016; Arora, 2003). CLASSIC v1.0 is described and evaluated by Melton et al., (2020) and Seiler et al., (2021). A detailed
140 description of model updates and improvements to CLASSIC since v1.0 that are utilized by our simulations can be found in
141 Asaadi et al. (2018), MacKay et al. (2022), and Curasi et al. (2022). We carry out simulations of the pan-Canadian domain
142 using a parameterization of the model which includes Canada-specific plant functional types (PFTs) that were developed and
143 evaluated by Curasi et al., (2022).

144
145 The CTEM dynamic vegetation sub-model simulates photosynthetic fluxes, at a thirty-minute time step in offline simulations,
146 and the allocation of C within live vegetation to structural and non-structural components of leaves, stems, and roots at a daily
147 time step. CTEM also simulates daily autotrophic respiration from leaves, stems, and roots and heterotrophic respiration fluxes
148 from litter and soil C. The pan-Canadian parameterization of CTEM utilizes fourteen biogeochemical PFTs (Curasi et al.,
149 2022). CTEM is coupled to CLASS on a daily time step and provides CLASS with vegetation height, leaf area index, biomass,
150 and rooting depth. CLASS, in turn, provides CTEM with mean daily soil moisture, soil temperature, and net radiation incident
151 on the land surface. CLASS simulates ground and canopy energy exchange from four possible subareas: bare ground, snow-
152 covered bare ground, canopy-covered ground, and snow-covered canopy, on a thirty-minute time step. It uses 20 ground layers
153 from 0.1 m to 30 m thick to a depth of over 61 m and simulates heat transfer within all permeable soil layers and the underlying
154 bedrock. It also simulates water fluxes between the soil layers up until the depth of the impermeable bedrock layer, derived
155 from Shangguan et al. (2017). CLASS models a single-layer canopy and uses five physics PFTs, which map directly onto the
156 14 CTEM biogeochemical PFTs, in the pan-Canadian parameterization (Curasi et al., 2022).

157 **2.3 Dynamic tile representation of externally forced fire and harvest**

158 **2.3.1 The composite versus mosaic representation in CLASSIC**

159 CLASSIC can utilize either a composite (1 tile) or mosaic (>1 tile) representation of the land surface. The composite
160 representation simulates average individual PFTs for each grid cell and uses their average structural attributes (i.e. leaf area

161 index, height, and rooting depth) to simulate the energy balance, and physical environment (i.e. soil temperature). The
162 structural attributes of all of the average individual PFTs that exist within a grid cell are averaged in proportion to their
163 fractional coverages and the PFTs all experience a common land surface physical environment. For the composite
164 representation, a disturbance event (i.e. wood harvest) takes C from the average individual PFTs pools proportional to the areal
165 fraction disturbed (i.e. a complete harvest of 50% of the grid cell thereby removing 50% of the vegetation biomass; Figure 1).

166
167 The mosaic representation splits the grid cell into multiple tiles representing fractional areas of the grid cell. Each tile receives
168 the same meteorological forcing but simulates its respective average individual of each PFT present, PFT structural attributes,
169 and energy balance. The structural attributes of all the average individual PFTs that exist within each tile are averaged in
170 proportion to their fractional coverages and the PFTs all experience a land surface physical environment common to that tile.
171 The tiles are aggregated to the scale of the final model grid by accounting for each tile's fractional coverage of the grid cell.
172 CLASSICs tiling capability has been used in the past to investigate the impacts of subgrid-scale heterogeneity in soil texture
173 by breaking grid cells with heterogeneous soil textures into tiles (Melton et al., 2017). As well as vegetation cover (Melton
174 and Arora, 2014; Li and Arora, 2012), and competition between plant functional types (Shrestha et al., 2016) by breaking grid
175 cells with heterogeneous vegetation cover into tiles. These approaches result in regional differences in fluxes of up to 30%.
176 We adapt the mosaic representation to dynamically create disturbance history tiles and represent the subgrid-scale
177 heterogeneity resulting from disturbance (i.e. represent a complete harvest of an area corresponding to 50% of the grid cell as
178 a 100% reduction of the vegetation biomass in a new subgrid tile that covers 50% of the grid cell; Figure 1). In our approach,
179 the tiles serve to represent vegetation that is in different stages of recovery. Thus, the soil textures and vegetation fractional
180 cover are the same for all tiles within a given grid cell.

181 **2.3.2 Notation and background**

182 We present generalized equations that illustrate the dynamic tiling calculations done by the model to split and join tiles. In
183 these equations, scalars are lowercase letters (i.e. $x = [1]$), vectors are bold lowercase letters (i.e. $\mathbf{x} = [x_1, x_2, \dots, x_n]$), and

184 matrices are bold uppercase letters (i.e. $\mathbf{X} = \begin{pmatrix} x_{1,1} & \cdots & x_{1,n} \\ \vdots & \ddots & \vdots \\ x_{n,1} & \cdots & x_{n,n} \end{pmatrix}$). The model is set up to simulate state variables for a user-

185 defined maximum number of tiles within a grid cell (i.e. the state variable \mathbf{x}_{all} with a length equal to the user-determined
186 maximum number of tiles). Tiles can be set as either active or inactive in each timestep (Figure 1). When the model identifies
187 active tiles for merging or splitting (e.g. sections 2.3.4, 2.3.5, and 2.3.6) they become candidate tiles. Depending upon the
188 operation and the fraction of the grid cell involved, anywhere between one and the total number of tiles being actively simulated
189 are candidate tiles for the merging or splitting operation. Because the maximum number of tiles is fixed, the model must
190 manage the number of tiles being actively simulated. The model ensures that up to two inactive tiles are available to simulate
191 disturbance each year (i.e. one for fire and one for harvest; see section 2.3.4). During the merging or splitting operation the

192 model temporarily stores values from the candidate tiles before the operation (i.e. \mathbf{x}_{pre} of length n candidate tiles) and after the
 193 operation (i.e. \mathbf{x}_{post} of length n candidate tiles) and uses them to calculate the values for a new single output tile (i.e. x_{new}). All
 194 these values are temporarily stored and used in calculations up until the point where the dynamic tiling operation is complete,
 195 and the model's main data structures are updated.

196

197 **2.3.3 Dynamic tiling splits and joins**

198 Dynamic tiling allows the model to split grid cells into subgrid tiles during the model run or join existing subgrid tiles. Dynamic
 199 tiling operations (splitting/joining) occur on January 1st at the annual time step alongside rigorous checks to ensure water,
 200 mass, and energy conservation. The area occupied by a given tile is a fraction of the grid cell land area between zero and one
 201 (i.e. \mathbf{a}_{all} with length equal to the user-determined maximum number of tiles). The sum of \mathbf{a}_{all} for all the active tiles within a
 202 grid cell must equal one. When tiles are split the fractional area occupied by the single new tile (a_{new}) must be less than the
 203 sum of the vector of fractional areas of the candidate tiles (\mathbf{a}_{pre} of length n candidate tiles). The candidate tiles' fractional areas
 204 are a product of the dynamic tiling operations that occur in all previous time steps. When the first dynamic tiling operation in
 205 a run occurs $a_{pre} = [1]$, but \mathbf{a}_{pre} is a much more complex vector in subsequent operations (e.g. $\mathbf{a}_{pre} = [0.1, 0.2, 0.3]$). The
 206 candidate tiles are later assigned a vector of new fractional areas adjusted to account for the new tile and the decrease in size
 207 of the candidate tiles (\mathbf{a}_{post} also of length n candidate tiles; Eqn. 1).

$$208 \quad a_{new} < \sum_{i=1}^n a_{pre,i}$$

$$209 \quad a_{post,n} = a_{pre,n} - a_{new} \frac{a_{pre,n}}{\sum_{i=1}^n a_{pre,i}} \quad (1)$$

210 When tiles are joined by the model the fractional area of the new tile is the sum of the vector of the fractional areas of the
 211 candidate tiles. The candidate tiles are later assigned fractional areas of zero (Eqn. 2).

$$212 \quad a_{new} = \sum_{i=1}^n a_{pre,i}$$

$$213 \quad a_{post} = 0 \quad (2)$$

214 For a tile or group of tiles to be split or joined they must pass rigorous checks that ensure they share the same abiotic
 215 characteristics and static fractional PFT cover. These characteristics (i.e. soil texture, soil permeable depth, and PFT fractional
 216 coverage) are copied directly to the new tile by the split or join. Mass-based variables (i.e. vegetation C pool mass, soil C pool
 217 mass, soil water, ponded water, and water held in the vegetation canopy) are split or joined using fractional area-based weighted
 218 averages to ensure mass balance. The value of the mass-based variable in the new tile (\mathbf{M}_{new} for l layers and o PFTs; kg m^{-2})
 219 is the average of the values for the candidate tiles (\mathbf{M}_{pre} of length n candidate tiles for l layers and o PFTs; kg m^{-2}) weighted
 220 by the fractional areas of the candidate tiles (Eqn. 3).

$$m_{new,lo} = \frac{\sum_{i=1}^n m_{pre,ilo} a_{pre,i}}{\sum_{i=1}^n a_{pre,i}} \quad (3)$$

Temperature-based variables (i.e. temperatures of the vegetation canopy, ponded water, snowpack, and soil) are split or joined using a fractional area-based weighted average that blends the different temperature materials from the candidate tiles. The value of a given temperature for the new tile (t_{new} for l layers; K) is a function of the temperatures in the candidate tiles (\mathbf{T}_{pre} of length n candidate tiles for l layers; K) weighted by the fractional areas of the candidate tiles before the split, the masses of the pools which track that temperature (\mathbf{M}_{pre} of length n candidate tiles for l layers and m pools; kg m⁻²), and the specific heat capacities which characterize those mass pools (\mathbf{c} for m pools; J kg⁻¹ K⁻¹; Eqn. 4).

$$t_{new,l} = \frac{\sum_{i=1}^n (t_{pre,il} a_{pre,i} \sum_{j=1}^m (m_{pre,ilj} c_j))}{\sum_{i=1}^n (a_{pre,i} \sum_{j=1}^m (m_{pre,ilj} c_j))} \quad (4)$$

2.3.4 Dynamic tiling management

The maximum number of dynamic tiles in a given simulation is limited by a parameter set at the start of the model run. If this upper limit is reached, tiles are joined based on a similarity criteria. By default, the model selects the two tiles with the most similar vegetation heights and joins them. The model uses the vector of tile average vegetation heights (\mathbf{h} of length n for a total number of tiles; m) and calculates the absolute difference between all possible combinations of the elements therein (i.e. using the nested iterators $n1$ and $n2$). The resulting absolute difference matrix of tile average vegetation heights ($\Delta\mathbf{H}$ a $n1$ total number of tiles by $n2$ total number of tiles matrix; m) is used to judge the similarity between tiles. The tile average vegetation height is a function of each PFT height (\mathbf{H} of length n total number of tiles for o PFTs; m) and the PFT fractional coverage within the tile (\mathbf{F} of length n total number of tiles for o PFTs; Eqn 5; Figure S1). In the default case, the two tiles with the minimum $\Delta\mathbf{H}$ are joined when the maximum number of dynamic tiles is reached.

$$\Delta\mathbf{h}_{n1,n2} = |\mathbf{h}_{n1} - \mathbf{h}_{n2}|$$

$$\mathbf{h}_n = \frac{\sum_{o=1}^{\# \text{ of PFTs}} h_{n,o} f_{n,o}}{\sum_{o=1}^{\# \text{ of PFTs}} f_{n,o}} \quad (5)$$

An optional relative height threshold (rht ; unitless) allows for tiles to be pre-emptively joined at a yearly time step before reaching the maximum number of dynamic tiles. The rht can be conceptually thought of as breaking the tiles into equally spaced bins organized by vegetation height. It is used to calculate a threshold value from the maximum tile average vegetation height (\mathbf{h} ; m). The threshold logically determines which pairs of tiles are pre-emptively joined at a yearly time step based on the absolute differences in their tile average vegetation heights ($\Delta\mathbf{H}$; m; Eqn 6; Figure S1).

$$\Delta\mathbf{H} < rht * \max(\mathbf{h}) \quad (6)$$

When the rht parameter is used, the optional tile preservation parameter (tpp ; number of tiles) prevents tiles with the shortest average vegetation height from being merged. That is the model, starting with the tile with the shortest average vegetation height, retains that number of tiles, tpp . This means the tiling scheme will carry out pre-emptive joins based upon rht while preserving young recently disturbed tiles and explicitly representing early successional differences in fluxes (Bellassen et al., 2010; Zaehle et al., 2006; Nabel et al., 2020). When dynamic tiling is active, the time since disturbance is tracked in all tiles.

252 Time since disturbance increases at the CTEM timestep (i.e. daily). Any disturbance events applied to a particular tile resets
253 its time since disturbance to zero.

254

255 **2.3.5 Externally forced fire**

256 Externally forced fire builds upon the pre-existing fire module within CLASSIC (Melton and Arora, 2016; Arora and Melton,
257 2018). The annual fractional burned area in a grid cell is read from a file. The model assumes that fire impacts all non-crop
258 PFTs.

259

260 If dynamic tiling is not active, biomass from the average individual and the litter pool burns proportional to the requested
261 fractional burned area. If dynamic tiling is active, a new tile with a fractional area equal to the fractional burned area is split
262 from the active tiles within the grid cell and subsequently burned. Depending upon the requested fractional burned area and
263 the conditions in the grid cell the model uses anywhere between one and the total number of tiles being actively simulated as
264 candidate tiles for this splitting operation.

265

266 To determine the candidate tiles for this splitting operation, the model ranks the tiles based on their probability of fire (\mathbf{p} of
267 length n) conditional on the total aboveground biomasses available for burning (\mathbf{b} of length n ; kg C m^{-2}). \mathbf{p} is a linear function
268 of the lower biomass threshold (0.4 kg C m^{-2}) under which fire cannot sustain itself and the upper biomass threshold over
269 which fire has a probability of one (1.2 kg C m^{-2} ; Eqn. 7) (Moorcroft et al., 2001; Kucharik et al., 2000; Melton and Arora,
270 2016).

$$271 \quad p_n = \max \left[0, \min \left(1, \frac{b_n - 0.4}{1.2 - 0.4} \right) \right] \quad (7)$$

272 The model initially selects tiles with a p of one as candidate tiles to be split to yield the tile to be burned. However, if these
273 selected tiles do not contain enough fractional area to simulate the fractional burned area requested, the model selects tiles with
274 a p less than one from largest to smallest (Figure S1). Externally forced fire uses a single probability (\mathbf{p}) to rank tiles, whereas
275 CLASSIC's standard fire module uses three probabilities to calculate the burned area: the probability of fire conditional on
276 total aboveground biomasses available for burning, the combustibility of the fuel based on its moisture content, and the
277 presence of an ignition source (Arora and Boer, 2005; Arora and Melton, 2018). We make this simplification here because the
278 fractional burned area comes from a file and all the tiles within a grid cell experience the same driving meteorology limiting
279 differences in moisture content and ignition (Melton et al., 2017; Melton and Arora, 2014). With either dynamic tiling active
280 or inactive, we calculate the C emissions to the atmosphere using pre-defined PFT-specific fire emission fractions for each
281 live vegetation component (i.e. both structural and non-structural leaves, stems, and roots) as well as the litter pool (θ ; Table
282 1). We calculate the quantity of live vegetation C transferred to the litter pool as a result of fire-related mortality using pre-
283 defined PFT-specific mortality fractions (Θ ; Table 1). Externally forced fire does not impact crop PFTs and thus their biomass
284 never combusts nor experiences fire-related mortality.

286 **2.3.6 Externally forced harvest**

287 Harvest simulates the removal of biomass from the landscape because of logging activities and builds upon the pre-existing
288 land use change module within CLASSIC (Arora and Boer, 2010). The annual fractional harvested area on a per grid cell basis
289 is read from a file. The model assumes that all harvest events are clear-cuts that impact some fraction of the simulated grid
290 cell.

291
292 If dynamic tiling is not active, the average individual is harvested proportional to the requested fractional area. If dynamic
293 tiling is active, a new tile with a fractional area equal to the requested fractional area is split from the oldest undisturbed active
294 tile, and the entire new tile is harvested. If the harvested area requested exceeds the fractional area of the oldest undisturbed
295 active tile the model selects additional active tiles as candidate tiles from oldest to youngest until there is sufficient fractional
296 area.

297
298 In either case, the harvested aboveground biomass (i.e. both non-structural and structural stem and leaf C) is split into three
299 streams using fractions developed by Arora and Boer 2010. These streams contribute C to the atmosphere, slash/pulp and
300 paper products pool, and durable wood products pool. The fractions of harvested aboveground biomass allocated to each stream
301 (ϵ ; Table 2) depend upon whether the PFT is woody or herbaceous and in the case of woody PFTs the aboveground biomass
302 density. Unlike the procedure described by Arora and Boer (2010) where root biomass is transferred to the slash/pulp and
303 paper products pool, we transfer harvested root biomass to the applicable PFT and soil depth-specific litter pools.

304

305 **2.4 Model forcing**

306 2.4.1 Meteorological drivers and landcover

307 CLASSIC requires seven meteorological forcing variables: incoming shortwave radiation, incoming longwave radiation, air
308 temperature, precipitation rate, air pressure, specific humidity, and wind speed. We use the interpolated and disaggregated
309 meteorological forcing described in detail by Meyer et al. (2021) and Curasi et al. (2022) (GSWP3–W5E5–ERA5) in our
310 simulations. The 1901 – 1978 portion of the forcing comes from the Inter-Sectoral Impact Model Intercomparison Project
311 GSWP3–W5E5 and the 1979–2018 portion comes from the ERA5 time series bias corrected to match the means of the
312 overlapping period in the GSWP3–W5E5 (Kim, 2017; Lange, 2019, 2020a, b; ECMWF, 2019). The atmospheric CO₂
313 concentrations (1700 - 2017) were obtained from the global carbon project (Trends in atmospheric carbon dioxide, National
314 Oceanic & Atmospheric Administration, Earth System Research Laboratory (NOAA/ESRL), 2022; Friedlingstein et al., 2022).

315

316 We set the fractional coverage of PFTs using the remotely sensed 14 PFT-hybrid land cover product generated by Wang et al.
317 (2022) and expanded upon and evaluated by Curasi et al. (2022). This land cover corresponds to the year 2010. This land cover
318 product combines information from the North American Land Change Monitoring System land cover (Latifovic et al., 2017),
319 the National Terrestrial Ecosystem Monitoring System (NTEMS)(Hermosilla et al., 2018, 2016), satellite-derived maps of the
320 National Forest Inventory attributes (Beaudoin et al., 2018), and British Columbia’s biogeoclimatic ecosystem classification
321 map (MacKenzie and Meidinger, 2018; Salkfield et al., 2016). Using a land cover that does not vary in time (i.e. static land
322 cover as opposed to dynamic or prescribed land cover changes) allows us to focus on the influence of fire, harvest, and dynamic
323 tiling on the model outputs.

324

325 2.4.2. Fire and harvest forcing

326 We develop fire and harvest drivers that detail the per-grid cell annual fractional area harvested or burned between 1740 and
327 2017 (Figure 2a, b). For the satellite era (1985 - 2017) we use remotely sensed 30-m spatial resolution records of harvest and
328 fire events. These data were derived from Landsat by using breakpoint detection to identify changes and trends (Hermosilla et
329 al., 2016, 2015a), followed by a random forest classification of change types (Hermosilla et al., 2015b). We mask the remotely
330 sensed harvest records to include only private, long-term tenure, and short-term tenure forests, as indicated by Stinson et al.,
331 (2019).

332

333 Before the availability of the remotely sensed records used herein (pre-1984), to our knowledge, there are no spatially explicit
334 pan-Canadian integrated harvest and fire data sets available. Therefore, to represent the impact of historical disturbance on the
335 model state we employ established methods for inferring disturbance events from stand age (Nabel et al., 2020; Kurz et al.,
336 2009; Chen et al., 2000, 2003). We also focus our analysis of the CLASSIC simulations on the satellite era (1985 - 2017) due
337 to uncertainties in inferred historical disturbance and the model state before the satellite era. Maltman et al., (2023) derived a
338 30-m resolution stand age map for 2019 from Landsat and MODIS data utilizing three methods. The methods included
339 disturbance detection for stands between 0 and 34 years of age, detection of spectral signals indicative of recovery for stands
340 between 34 and 54 years of age, and inverting allometric equations for stands between 54 and 150 years of age. We infer the
341 year in which the last disturbance occurred from the stand age. For example, a 40-year-old forest in 2019 is assumed to have
342 been last disturbed in 1979. We use regional averages of the per-pixel ratio of burned to total disturbed area from the first
343 decades of the satellite era (1985 - 1995) to fraction total inferred disturbance into fire and harvest.

344

345 However, pre-1984 disturbance that has been inferred from stand age does not align with available aspatial records of total
346 harvested and burned area within Canada. Therefore, we utilize the aspatial records to bias-correct the 1740 – 1984 disturbance
347 that has been inferred from stand age to ensure the total values match the available historical records. From 1740 - 1920, we
348 utilized aspatial records of total disturbed area derived from 1920 stand age, with harvest held constant (0.3 Mha yr^{-1}) (Chen
349 et al., 2000; Kurz et al., 1995). From 1920 – 1984 we utilized aspatial records of the total harvested and burned area within

350 Canada from Skakun et al., (2021) and World Resources Institute (2000). We utilize bias correction that retains the spatial
 351 patterns of pre-1984 disturbance inferred from stand age while correcting positive and negative biases to match the aspatial
 352 records. This necessitated two distinct bias correction methods. For years with positive biases, the positive bias indicates that
 353 there is sufficient disturbance inferred from stand age. In these cases, a uniform bias correction factor can be used to scale
 354 down disturbance. Years with negative biases, however, do not contain sufficient disturbance as inferred from stand age. Here
 355 residual disturbed area from nearby years needs to be added to the year under consideration to match the aspatial records level
 356 of disturbance while preserving the spatial patterns derived from stand age. Because the uncertainty of stand age estimates
 357 increases further into the past, the negative bias correction is carried out starting in 1984 and looping backward annually until
 358 1740 (Maltman et al., 2023).

359
 360 First, for years in which burned or harvested area inferred from stand age ($\mathbf{D}_{\text{inferred}}$ for i years, l grid cells; m^2) exceeded the
 361 aspatial records ($\mathbf{d}_{\text{aspatial}}$ for i years; m^2) we correct the positive biases. We calculate an aspatial bias-correction factor (f for i
 362 years; unitless; eqn. 8).

$$363 \quad f_i = \frac{\left(\left(\sum_{l=1}^{\# \text{ of grid cells}} d_{\text{inferred},i,l} \right) - d_{\text{aspatial},i} \right)}{\left(\sum_{l=1}^{\# \text{ of grid cells}} d_{\text{inferred},i,l} \right)} \quad (8)$$

364 Because the pre-1985 records are aspatial, the bias correction factor is temporally explicit but uniformly applied across space.
 365 When we apply the bias-correction factor to the inferred disturbance time series the result is a new time series with all the
 366 positive biases corrected ($\mathbf{D}_{\text{downsc}}$ for i years, l grid cells; m^2 ; eqn. 9).

$$367 \quad d_{\text{downsc},il} = d_{\text{inferred},il} - d_{\text{inferred},il} f_i \quad (9)$$

368 When we apply the bias-correction factor we retain the spatially and temporally explicit residuals ($\mathbf{D}_{\text{residual}}$ for i years, l grid
 369 cells; m^2 ; eqn. 10).

$$370 \quad d_{\text{residual},il} = d_{\text{inferred},il} - d_{\text{downsc},il} \quad (10)$$

371 Second, for years in which burned or harvested area inferred from stand age falls below that indicated in the aspatial records,
 372 we correct the negative biases by adding in the residuals from nearby years (Figure 3). We loop backward in time from 1984
 373 to 1740 and accumulate residuals ($\mathbf{r}_{\text{moving}}$ for l grid cells; m^2) extending as far back in time as needed to exceed the aspatial
 374 record for the year under consideration ($\mathbf{d}_{\text{aspatial},i}$). We calculate an aspatial bias-correction factor (f ; unitless) and use it to apply
 375 a fraction of $\mathbf{r}_{\text{moving}}$, to the inferred disturbance time series and subtract the residuals used from $\mathbf{r}_{\text{moving}}$. When the spatially
 376 explicit residuals are exhausted (~ 1920 for fire only) they are replenished using the entire gridded remotely sensed and stand
 377 age inferred disturbance record. This procedure continues until all the negative biases have been corrected between 1984 and
 378 1740 yielding the final spatially explicit time series ($\mathbf{D}_{\text{final}}$ for i years, l grid cells; m^2).

379

380 **2.5 Simulation protocol**

381 We carry out a total of fourteen simulations using a common simulation protocol to investigate the impact of different
382 maximum numbers of available tiles, *rht*, and *tpp* (Table 3). *rht* (0.04 - 0.16, unitless) can be conceptually thought of as
383 breaking the range of tile average vegetation heights into between 24 and 6 equally spaced bins depending upon its value (e.g.
384 (1 bin $\text{m m}^{-1} / 6 \text{ bins}$) = 0.16 m m^{-1}). *tpp* (4 - 6 tiles) can be conceptually thought of as the maximum number of discrete
385 disturbance events that the model can simulate in a grid cell over 2 - 3 years (e.g. (1 harvest tile yr^{-1} + 1 fire tile yr^{-1}) * 3 yrs
386 = 6 tiles).

387
388 We spin up the model to equilibrium conditions corresponding to the year 1700 and then do a transient run over the period
389 1700 to 2017. For the spin up we loop the earliest 25 years of climate data available (1901 - 1925) and hold atmospheric CO_2
390 concentrations constant at the pre-industrial (1700) level. The 1700 - 1900 portion of the transient run uses the same loop of
391 1901 - 1925 climate, but transient atmospheric CO_2 concentrations. The 1900 - 2017 portion of the transient run uses transient
392 atmospheric CO_2 concentrations and evolving GSWP3–W5E5–ERA5 climate. During the full transient simulation from 1740
393 - 2017, the fire and harvest are applied (see Section 2.4). The 14 transient simulations utilize their individual unique, lang
394 surface representation (i.e. composite or mosaic) maximum number of available tiles, *rht*, and *tpp* for the entire 1700 – 2017
395 run (Table 3). The CLASSIC nitrogen cycling module is not active in these simulations (Asaadi and Arora, 2021; Arora and
396 Boer, 2010).

397 **2.6 Model evaluation**

398 We carry out model-on-model comparisons for a selection of variables and model configurations for the satellite era portions
399 of our simulations (1985 - 2017) to select the model setup that optimally balances detailed process representation and model
400 run time (Table 3). This model-on-model approach has the benefit of canceling out any pre-existing biases in the model and
401 focuses our results on the impacts of subgrid-scale heterogeneity, and discretization error alone (similar to Torres-Rojas et al.,
402 2022; Moorcroft et al., 2001). We also use these evaluations to demonstrate the relative impact of representing subgrid-scale
403 heterogeneity within our modeling framework. We evaluate a suite of C cycling and surface energy balance-related variables
404 including the land carbon pool (cLand), vegetation C (cVeg), soil C (cSoil), gross primary productivity (GPP), autotrophic
405 respiration (Ra), heterotrophic respiration (Rh), ecosystem respiration (ER), leaf area index (LAI), sensible heat flux (HFSS),
406 latent heat flux (HFSL), albedo (ALBS), fire emissions (fFire), total deforested C (fDeforestTotal), and cumulative deforested
407 C (the running sum of fDeforestTotal starting in 1985; fDeforestCumulative).

408
409 To select the optimal maximum number of tiles available for the simulation as well as the *rht* and *tpp* we calculate the mean
410 squared deviation (**msd** for *j* model runs detailed in Table 3 over the 1985 - 2017 period) between the model runs under
411 evaluation and the reference 32-tile run. The 32-tile run is the reference point as it is the simulation with the least compromise

412 between runtime and simulation detail and is assumed to best represent the impacts of disturbance in CLASSIC. msd is the
 413 mean of the squared differences between the annual summary (i.e. means for fluxes and sums for pools) of each variable for
 414 the 32-tile run ($\hat{\mathbf{x}}_{32tile}$ containing i years) and that for the simulations under evaluation ($\hat{\mathbf{X}}$ containing i years for j model runs;
 415 Eqn 11).

$$416 \quad msd_j = \frac{1}{33} \sum_{i=1985}^{2017} (\hat{x}_{j,i} - \hat{x}_{32tile,i})^2 \quad (11)$$

417 We also use a normalized response metric ($\Delta\bar{\mathbf{X}}_{norm}$ for, j model runs, k variables; Eqn 12) to evaluate the relative impacts of
 418 disturbance and subgrid-scale heterogeneity on the simulations. The normalized response metric is a unitless summary statistic.
 419 It's strength is that a wide range of variables with different units can be visualized on the same axis to make relative
 420 comparisons of their simulated responses to disturbance and tiling. For a given variable, the metric normalizes each variable's
 421 output (\mathbf{X} for i years, j model runs, k variables, l grid cells) using the minimum and maximum across all the outputs (\mathbf{X}_{norm} for
 422 i years, j model runs, k variables, l grid cells; Eqn 12). Each normalized variable is averaged across the model domain and run
 423 years ($\bar{\mathbf{X}}_{norm}$ for, j model runs, k variables; 1985 - 2017) considering each model grid cell's area ($a_{grid\ cell}$; m^2). Finally, the
 424 absolute value of the difference between $\bar{\mathbf{X}}_{norm}$ for the desired runs (1-tile/not-disturbed, and 32-tile run) and the 1-tile/disturbed
 425 run is calculated (Eqn 12).

$$426 \quad x_{norm,i,j,k,l} = \frac{(x_{i,j,k,l} - \min(X_k))}{(\max(X_k) - \min(X_k))}$$

$$427 \quad \bar{x}_{norm,j,k} = \frac{\sum_{i=1985}^{2017} (\sum_{l=1}^{\# \text{ of grid cells}} x_{norm,i,j,k,l} a_{grid\ cell,l})}{33 (\sum_{l=1}^{\# \text{ of grid cells}} a_{grid\ cell,l})}$$

$$428 \quad \Delta\bar{x}_{norm,j,k} = |\bar{x}_{norm,j,k} - \bar{x}_{norm,1-tile/disturbed,k}| \quad (12)$$

429 All plots are created using R or the External Dynamic and Interactive Framework Integrating CLASSIC Experiments
 430 (EDIFICE) Python suite (Hijmans et al., 2015; R core team, 2013).

431 3. Results and discussion

432 3.1 Disturbance events within Canada

433 For the period represented by satellite data in this study, the highest total disturbed areas are in central boreal regions of the
 434 country and are attributable to wildfire events (Figure 2c). In contrast, harvest concentrates on the west coast and eastern boreal
 435 and maritime regions of the country. The annual total disturbed area differs widely between years during the satellite era
 436 (Figure 2a,b). In aggregate, harvest occurs in ~2% of the land area modeled, and fire occurs in ~6% from 1985 to 2017. The
 437 total number of simulated disturbance events is moderate with 89% of the grid cells incorporating 32 or fewer simulated
 438 disturbance events during the satellite era and 61% incorporating 11 or fewer (Figure 2d,e). Our aspatial tiling scheme operates
 439 on an annual timestep and therefore the maximum number of possible events in the 1985 - 2017 drivers is 66 (i.e. a harvest

440 and fire each year for 33 years; Figure 2e). Generally, beyond 11 simulated disturbance events, there is a limited correlation
441 between the number of simulated disturbance events and the total area disturbed (Figure 2e).

442 **3.2 Model parameterization**

443 The change in the msd (Figures 4a-h) as the maximum number of available tiles for the run increases from 1 to 32 exhibits a
444 roughly exponential decline for surface energy balance (HFSS, HFSL) and C cycle-related variables (cLand, GPP, ER, LAI).
445 The msd is near zero at 7 – 12 tiles. The 32-tile simulation captures all the discrete disturbance events from 1985 - 2017 across
446 most of the model domain (Figure 2). However, a simulation that resolves all the disturbance events between 1740 and 2017
447 as tiles would require far more than 32 tiles, in many forested areas, and be computationally intractable. However, we infer
448 from the exponential (e.g. rather than linear) decreasing rate of change in Figures 4a-f that our reference 32-tile simulation has
449 minimal discretization error and converges on the results of that computationally intractable simulation (Torres-Rojas et al.,
450 2022; Nabel et al., 2020; Nocedal & Wright 2006). The difference in msd between the 32-tile tile simulation and that
451 computational intractable simulation would likely be vanishingly small, similar to the difference between the 25-tile and 32-
452 tile simulations (Nabel et al., 2020; Fisher et al., 2018; Ellner and Guckenheimer, 2011; Gelman and Hill, 2006). These roughly
453 exponential declines in msd reflect the model's ability to discretize patches of vegetation in different stages of recovery using
454 greater numbers of tiles. This is reflected in how the statistical distributions of aboveground tree biomass in forested grid cells
455 change as more tiles are utilized in the simulation (Figure 5a).

456
457 Disturbance-related variables including fFire, as well as fDeforestedTotal exhibit a less sharp decline when going from one to
458 seven tiles and approaches zero at 12 tiles (Figures 4g-h). This reflects the role of selecting and splitting tiles in different phases
459 of recovery on these processes and the extent to which recovering tiles with lower aboveground tree biomass are represented
460 in the simulation (Figure 5a). As a result, there is a discontinuity between representing these processes using average
461 individuals, a small number of highly heterogeneous tiles, and many tiles (Figures 4g-h, 5a). This pattern is also likely
462 influenced by the relatively low magnitude of the differences between the simulations when, compared to the fluxes themselves
463 (Figure 6a,h,i).

464
465 The run time for the satellite-era simulation (1985 - 2017) with 1-tile is ~318 CPU hours (i.e. the sum of time utilized by all
466 cores across multiple machines; Xeon Platinum 8380). Compared to the 1-tile run, the 32-tile run, 12-tile and optimized runs
467 consume 14 times, 3 times, and 2 times as many CPU hours respectively. The run time of the simulations increases linearly
468 between one and twelve tiles (Figure 4i) but increases more rapidly from eighteen to thirty-two tiles due to the increasingly
469 large multidimensional per-tile structures in memory. The intercept (i.e. the overhead for pre-processing meteorological files
470 and initializing MPI sessions to run the model with a single tile) is around three times the slope (i.e. the time required to run
471 each additional tile) for simulations with less than 12 tiles. This suggests that the splitting operations involved in simulating
472 additional tiles are computationally efficient and do not dramatically increase the run time (Nabel et al., 2020).

473

474 As with all modeling exercises, we must balance model accuracy, complexity, and computational efficiency. We, therefore,
475 use simulations with 12 tiles to set the *rht* (i.e. the relative height threshold for preemptively joining tiles) and *tpp* (i.e. the
476 number of preserved recently disturbed tiles) parameter values. Simulations using 12 tiles and different *rht* and *tpp* parameters
477 are very similar in terms of run time, and surface energy balance and C cycle-related variables exhibit no consistent patterns
478 (Figures S2a-f, i). There is a gradual increase in *msd* for *fFire* and *fDeforestedTotal* as *rht* and *tpp* increase (Figures S2g-h).
479 However, these differences are again of relatively low magnitude, compared to the fluxes themselves (Figure 6a,h,i). Therefore,
480 we chose an *rht* of 0.16 and a *tpp* of 4 to maximize computation efficiency. The optimal parameterization has *msd* values
481 similar to those of a run with twelve tiles, but at a lower run time (~23% less; Figure 4i). The optimal model nearly
482 approximates the heterogeneous tile structure of the more complex 32-tile simulation and represents forested areas with low
483 aboveground tree biomass like the 32-tile simulation, in line with observations of aboveground tree biomass from the NFI
484 (Figure 5b). However, it may over smooth the transition between low and high biomass areas (i.e. the ~2 - 3 gC m⁻² range in
485 Figure 5b) thereby impacting the size classes of the tiles selected for splitting during the disturbance simulation (Figure 4g-h).
486 Nonetheless, the optimal simulation effectively balances computational efficiency and discretization error.

487 **3.3 Impacts on simulated variables**

488 The response of the modeled variables to dynamic tiling (i.e. 1-tile/disturbed v.s. 32-tile, as illustrated in Figure 1, Table 3)
489 often meets or exceeds their response to disturbance alone (i.e. 1-tile/not-disturbed vs. 1-tile/disturbed; Figure 6a). The impact
490 of the optimal tiling scheme is minimal by comparison and, therefore, we focus on comparisons between the 1-tile/not-
491 disturbed, 1-tile/disturbed, and 32-tile outputs (Figures 6b-i, S3). C cycle-related variables including *cVeg*, and LAI show the
492 strongest response to disturbance, whereas energy balance-related variables including HFLS, HFSS, and ALBS show the
493 weaker responses. Many variables also respond strongly to dynamic tiling including LAI, Ra, and *cVeg* (Figure 6a,b,e). Select
494 surface energy balance-related variables including HFLS, HFSS, and ALBS respond more strongly to dynamic tiling than
495 disturbance alone (Figure 6a). These strong responses further reinforce the impact of disturbance-induced subgrid-scale
496 heterogeneity on ecosystem processes and the value of representing this heterogeneity within models (Bellassen et al., 2010;
497 Zaehle et al., 2006; Nabel et al., 2020; Körner, 2006; Dore et al., 2010; Luyssaert et al., 2014; Erb et al., 2017).

498

499 Disturbance-related variables such as *fFire* exhibit little difference with subgrid-scale heterogeneity (Figure 6h), whereas
500 *fDeforestCumulative* increases slightly (Figure 6i). These patterns occur as fire can potentially impact all subgrid stands above
501 a certain biomass threshold (Eqn. 7) while wood harvest preferentially impacts the tiles with the largest aboveground biomass
502 (i.e. approximating the highest quality tiles being harvested). Biomass removal by disturbance leads to a ~1.6 Pg decrease in
503 *cVeg* across Canada (an 8% decrease) while the subgrid level (tiled) representation of these processes leads to another ~1 Pg
504 decrease (Figure 6b). LAI mirrors these same patterns with a 4% decrease due to disturbance and another 4% decrease with
505 the subgrid level (tiled) representation (Figure 6e). As a result of disturbance, *cSoil* decreases at a higher rate from 1985 to

506 2017, whereas cVeg increases at very similar rates $\sim 0.035 \text{ Pg y}^{-1}$ (Figure 6b,c). For GPP and Ra, the impact of dynamic tiling
507 is $\sim 1.5 - 2.5$ times the impact of disturbance alone (Figure 6a,d). This offset in GPP and Ra is likely in part a product of
508 dynamic tiling simulating the naturally slower process of recovery from bare ground versus recovery of an average individual
509 with substantial pre-existing biomass and leaf area (Zaehle et al., 2006; Körner, 2006; Dore et al., 2010; Luysaert et al., 2014).
510 This slower recovery likely also contributes to the losses in cVeg between the 1-tile/disturbed and 32-tile simulation.

511
512 Dynamic tiling has impacts on HFLS, HFSS, and ALBS $\sim 1.5 - 4$ times the impact of disturbance alone (Figure 6a). The relative
513 impact on HFLS is the more muted of the three possibly because while removing vegetation causes a decrease in transpiration,
514 evaporation from the ground surface increases (Figure 6g). Dynamic tiling does appear to have larger impacts on ALBS where
515 the surface becomes brighter and by extension, HFSS decreases (Figure 6a,f). This occurs as the model with dynamic tiling is
516 capable of representing sparsely vegetated and often snow-covered fractions of the land surface as a result of recent disturbance
517 (Bright et al., 2013; Nabel et al., 2020). These impacts are muted or absent when disturbance is simulated by an average
518 individual model because only a proportion of the average individual's biomass is removed with enough remaining to support
519 a tall dense canopy that obscures the ground surface and recovers quickly.

520 **4. Conclusion: Implications for representing disturbance and subgrid-scale heterogeneity in LSMs**

521 The dynamic tiling scheme presented in this study could form the basis for a more detailed representation of land use change
522 and resultant subgrid-scale heterogeneity in CLASSIC, the land surface component of the LSM CanESM (Melton et al., 2020;
523 Seiler et al., 2021; Swart et al., 2019). Our tiling scheme has several advantages over other methods. It uses a relatively large
524 number of dynamic tiles as opposed to a small fixed number of tiles, which allows for a more granular representation of
525 vegetation recovery following disturbance (Shevliakova et al., 2009; Yue et al., 2018a; Naudts et al., 2015; Yang et al., 2010;
526 Stocker et al., 2014). It also explicitly simulates C and energy exchanges using tile average rather than grid cell average
527 properties thus fully simulating the impacts from the removal of vegetation by harvest or fire (Bellassen et al., 2010; Haverd
528 et al., 2014; Melton and Arora, 2014). Most importantly, the scheme is dynamic and has no designated size or age class bins;
529 the number of simulated tiles increases as disturbances occur and then are managed by on-demand or pre-emptive joins (Nabel
530 et al., 2020; Shevliakova et al., 2009; Naudts et al., 2015; Bellassen et al., 2010). The tiling routine adapts its size distribution
531 in response to lower disturbance frequencies, more extreme individual disturbance events, and potentially the addition of new
532 PFTs while remaining computationally efficient. Finally, the tiling scheme can preserve young, recently disturbed tiles which
533 may improve its representation of early successional differences in GPP, LAI, and cVeg (Bellassen et al., 2010; Zaehle et al.,
534 2006; Nabel et al., 2020). In the context of pan-Canadian or global offline simulations within CLASSIC, this dynamic tiling
535 scheme presents the opportunity for more detailed and efficient representations of LULCC than is achievable by simply
536 increasing the spatial resolution of the model, which is limited by model inputs such as meteorological forcing or coupling
537 considerations within CanESM. Future LULCC representations could implement more complex tile harvesting schemes to
538 represent forest management (i.e. thinning, re-planting, clearcut avoidance, or low-intensity harvest) (Puettmann et al., 2015;

539 Pan et al., 2010) or introduce tiles to account for new LULCC processes and states such as rangelands, pasture, fertilizer use,
540 and irrigation (Shevliakova et al., 2009). Other disturbances including insect damage, wind damage, and landslides could
541 likewise be represented using dynamic tiling. Insects in particular are an important disturbance agent in Canada that have more
542 spatially widespread impacts than fire and harvest, but greater variation in severity (Kurz et al., 2008; Chen et al., 2000). Non-
543 stand replacing impacts such as due to insect defoliation or drought stress can be detected, but determination of severity or
544 longer-term impacts remain difficult to quantify. Representing these disturbance events requires consistent spatially explicit
545 time series of the forcings, which are not widely available at present (Pongratz et al., 2018; Erb et al., 2017). This would also
546 require careful consideration of the impacts of the disturbance in question. We can infer from our results that low-severity non-
547 stand replacing disturbances may not require a tiled representation.

548

549 Finally, our model-on-model evaluation provides insights into the biases induced in specific variables by the absence of
550 dynamic tiling or particular dynamic tiling setups, which may apply to other similar tile-based LSMs/discretized schemes
551 (Nabel et al., 2020; Fisher et al., 2018). These results are strengthened by our model-on-model approach which acts to cancel
552 out pre-existing biases to demonstrate the impacts of subgrid-scale heterogeneity, and discretization error alone (Torres-Rojas
553 et al., 2022; Curasi et al., 2022; Melton et al., 2017; Melton & Arora 2014; Moorcroft et al., 2001). Representing subgrid-scale
554 stand structure leads to differences in land-use emissions if particular size or age classes within the grid cell are preferentially
555 impacted by fire or harvest (Nabel et al., 2020; Shevliakova et al., 2009; Yue et al., 2018b). Our results suggest that representing
556 a relatively small number of heterogeneous tiles may yield undesirable biases when compared to simulations using a larger
557 number of tiles (Figures 4a-h, 6a) (Yue et al., 2018a; Shevliakova et al., 2009; Stocker et al., 2014; Yang et al., 2010). For a
558 tile-based LSM to represent these subgrid impacts the simulation needs to be sufficiently complex and judiciously implemented
559 and tested. In the case of CLASSIC, we find that 7 – 12 tiles optimally balances detailed representation and computational
560 costs. An *rht* of 0.16 and a *tpp* of 4 increases computation efficiency with little impact on the level of detail represented.
561 Likewise, subgrid-scale stand structure impacts C fluxes, vegetation C stocks, and energy fluxes (Erb et al., 2017; Luysaert
562 et al., 2014; Körner, 2006; Dore et al., 2010). These subgrid-scale impacts can be of similar magnitude to the impacts of
563 disturbance alone, further reinforcing their significance (Figure 6).

564

565 Ultimately, Canadian forest ecosystems are critical components of the global C cycle which are responding to unprecedented
566 climate change. Quantifying historical disturbances and evaluating the impacts of different methods of representing
567 disturbance will improve the representation of the terrestrial C cycle in LSMs. This understanding will also facilitate a
568 comprehensive, process-based assessment of Canada's future terrestrial C cycle and its response to both disturbance events
569 and climate change.

570

571

572 **Code and data availability**

573 The Canadian Forest Service land cover and maps of forest disturbance described herein for Canada's forested ecosystems are
574 open access and are freely available at https://opendata.nfis.org/mapserver/nfis-change_eng.html. The Stinson et al., (2019)
575 forest management product is available through the Government of Canada's Open Data Portal
576 (<https://open.canada.ca/data/en/dataset/d8fa9a38-c4df-442a-8319-9bbcbdc29060>). The current version of CLASSIC is
577 available via the project website: <https://gitlab.com/cccma/classic>. The model version, additional software, setup files, and
578 outputs used herein are archived on Zenodo (<https://doi.org/10.5281/zenodo.8302974>).

579 **Author contributions**

580 S.R.C., J.R.M., and E.R.H. conceived of the analysis and methodology. S.R.C. conducted the formal analysis, visualization,
581 and software development, and wrote the original draft. J.R.M. and E.R.H. obtained funding for and oversaw the work. T.H.
582 and M.A.W. contributed the National Terrestrial Ecosystem Monitoring System data and to the disturbance-forcing
583 development. All authors contributed to writing and editing the manuscript.

584 **Competing interests**

585 The authors declare that they have no conflict of interest.

586 **Acknowledgments**

587 We would like to thank Mike Brady (ECCC) for his assistance in processing the disturbance data, Ed Chan for his assistance
588 with the model software and setting up the original model initialization files and meteorological drivers, and Libo Wang for
589 creating the original land cover products and cross-walking tables. We acknowledge the support of the Natural Sciences and
590 Engineering Research Council of Canada (NSERC), ALLRP 556430-2020. We also thank the anonymous reviewers for their
591 constructive comments.

592 **References**

593 Arora, V. K.: Simulating energy and carbon fluxes over winter wheat using coupled land surface and terrestrial ecosystem
594 models, *Agric. For. Meteorol.*, 118, 21–47, 2003.
595 Arora, V. K. and Boer, G. J.: Fire as an interactive component of dynamic vegetation models, *J. Geophys. Res.*, 110,
596 <https://doi.org/10.1029/2005jg000042>, 2005.

597 Arora, V. K. and Boer, G. J.: Uncertainties in the 20th century carbon budget associated with land use change, *Glob. Chang.*
598 *Biol.*, 16, 3327–3348, 2010.

599 Arora, V. K. and Melton, J. R.: Reduction in global area burned and wildfire emissions since 1930s enhances carbon uptake
600 by land, *Nat. Commun.*, 9, 1326, 2018.

601 Asaadi, Arora, Melton, and Bartlett: An improved parameterization of leaf area index (LAI) seasonality in the Canadian Land
602 Surface Scheme (CLASS) and Canadian Terrestrial Ecosystem ..., *Biogeosciences*, 2018.

603 Asaadi, A. and Arora, V. K.: Implementation of nitrogen cycle in the CLASSIC land model, *Biogeosciences*, 18, 669–706,
604 2021.

605 Babst, F., Bouriaud, O., Poulter, B., Trouet, V., Girardin, M. P., and Frank, D. C.: Twentieth century redistribution in climatic
606 drivers of global tree growth, *Sci Adv*, 5, eaat4313, 2019.

607 Beaudoin, A., Bernier, P. Y., Villemaire, P., Guindon, L., and Guo, X. J.: Tracking forest attributes across Canada between
608 2001 and 2011 using a k nearest neighbors mapping approach applied to MODIS imagery, *Can. J. For. Res.*, 48, 85–93, 2018.

609 Bellassen, V., Le Maire, G., Dhôte, J. F., Ciais, P., and Viovy, N.: Modelling forest management within a global vegetation
610 model—Part 1: Model structure and general behaviour, *Ecol. Modell.*, 221, 2458–2474, 2010.

611 Bond-Lamberty, B. and Gower, S. T.: Decomposition and Fragmentation of Coarse Woody Debris: Re-visiting a Boreal Black
612 Spruce Chronosequence, *Ecosystems*, 11, 831–840, 2008.

613 Böttcher, H., Kurz, W. A., and Freibauer, A.: Accounting of forest carbon sinks and sources under a future climate protocol—
614 factoring out past disturbance and management effects on age–class structure, *Environ. Sci. Policy*, 11, 669–686, 2008.

615 Bright, R. M., Astrup, R., and Strømman, A. H.: Empirical models of monthly and annual albedo in managed boreal forests of
616 interior Norway, *Clim. Change*, 120, 183–196, 2013.

617 Chaste, E., Girardin, M. P., Kaplan, J. O., Portier, J., Bergeron, Y., and Hély, C.: The pyrogeography of eastern boreal Canada
618 from 1901 to 2012 simulated with the LPJ-LMfire model, *Biogeosci. Discuss.*, 1–33, 2017.

619 Chen, J., Chen, W., Liu, J., Cihlar, J., and Gray, S.: Annual carbon balance of Canada’s forests during 1895-1996, *Global*
620 *Biogeochem. Cycles*, 14, 839–849, 2000.

621 Chen, J. M., Ju, W., Cihlar, J., Price, D., Liu, J., Chen, W., Pan, J., Black, A., and Barr, A.: Spatial distribution of carbon
622 sources and sinks in Canada’s forests, *Tellus B Chem. Phys. Meteorol.*, 55, 622–641, 2003.

623 Curasi, S. R., Melton, J. R., Humphreys, E. R., Wang, L., Seiler, C., Cannon, A., Chan, E., and Qu, B.: Evaluating the
624 performance of the Canadian Land Surface Scheme Including Biogeochemical Cycles (CLASSIC) tailored to the pan-
625 Canadian domain, *Earth and Space Science Open Archive*, <https://doi.org/10.1002/essoar.10512727.1>, 2022.

626 Czimczik, C. I., Trumbore, S. E., Carbone, M. S., and Winston, G. C.: Changing sources of soil respiration with time since
627 fire in a boreal forest, *Glob. Chang. Biol.*, 12, 957–971, 2006.

628 Trends in atmospheric carbon dioxide, National Oceanic & Atmospheric Administration, Earth System Research Laboratory
629 (NOAA/ESRL): <http://www.esrl.noaa.gov/gmd/ccgg/trends/global.html>, last access: 11 March 2022.

630 D'Orangeville, L., Houle, D., Duchesne, L., Phillips, R. P., Bergeron, Y., and Kneeshaw, D.: Beneficial effects of climate
631 warming on boreal tree growth may be transitory, *Nat. Commun.*, 9, 3213, 2018.

632 Dore, S., Kolb, T. E., Montes-Helu, M., Eckert, S. E., Sullivan, B. W., Hungate, B. A., Kaye, J. P., Hart, S. C., Koch, G. W.,
633 and Finkral, A.: Carbon and water fluxes from ponderosa pine forests disturbed by wildfire and thinning, *Ecol. Appl.*, 20, 663–
634 683, 2010.

635 ECMWF: ERA5 reanalysis (0.25 degree latitude-longitude grid), 2019.

636 Ellner, S. P. and Guckenheimer, J.: *Dynamic Models in Biology*, Princeton University Press, 2011.

637 Erb, K.-H., Luyssaert, S., Meyfroidt, P., Pongratz, J., Don, A., Kloster, S., Kuemmerle, T., Fetzel, T., Fuchs, R., Herold, M.,
638 Haberl, H., Jones, C. D., Marín-Spiotta, E., McCallum, I., Robertson, E., Seufert, V., Fritz, S., Valade, A., Wiltshire, A., and
639 Dolman, A. J.: Land management: data availability and process understanding for global change studies, *Glob. Chang. Biol.*,
640 23, 512–533, 2017.

641 Fisher, R. A., Koven, C. D., Anderegg, W. R. L., Christoffersen, B. O., Dietze, M. C., Farrior, C. E., Holm, J. A., Hurtt, G. C.,
642 Knox, R. G., Lawrence, P. J., Lichstein, J. W., Longo, M., Matheny, A. M., Medvigy, D., Muller-Landau, H. C., Powell, T.
643 L., Serbin, S. P., Sato, H., Shuman, J. K., Smith, B., Trugman, A. T., Viskari, T., Verbeeck, H., Weng, E., Xu, C., Xu, X.,
644 Zhang, T., and Moorcroft, P. R.: Vegetation demographics in Earth System Models: A review of progress and priorities, *Glob.*
645 *Chang. Biol.*, 24, 35–54, 2018.

646 Friedlingstein, P., Jones, M. W., O'Sullivan, M., Andrew, R. M., Hauck, J., Peters, G. P., Peters, W., Pongratz, J., Sitch, S.,
647 Le Quéré, C., and Others: Global Carbon Budget 2019, *Earth Syst. Sci. Data*, 11, 1783--1838, 2019.

648 Friedlingstein, P., Jones, M. W., O'Sullivan, M., Andrew, R. M., Bakker, D. C. E., Hauck, J., Le Quéré, C., Peters, G. P.,
649 Peters, W., Pongratz, J., and Others: Global carbon budget 2021, *Earth System Science Data*, 14, 1917–2005, 2022.

650 Gelman, A. and Hill, J.: *Data Analysis Using Regression and Multilevel/Hierarchical Models*, Cambridge University Press,
651 651 pp., 2006.

652 Gillis, M. D., Omule, A. Y., and Brierley, T.: Monitoring Canada's forests: The National Forest Inventory, *For. Chron.*, 81,
653 214–221, 2005.

654 Girardin, M. P., Bouriaud, O., Hogg, E. H., Kurz, W., Zimmermann, N. E., Metsaranta, J. M., de Jong, R., Frank, D. C., Esper,
655 J., Büntgen, U., Guo, X. J., and Bhatti, J.: No growth stimulation of Canada's boreal forest under half-century of combined
656 warming and CO₂ fertilization, *Proc. Natl. Acad. Sci. U. S. A.*, 113, E8406–E8414, 2016.

657 Goetz, S. J., Bunn, A. G., Fiske, G. J., and Houghton, R. A.: Satellite-observed photosynthetic trends across boreal North
658 America associated with climate and fire disturbance, *Proc. Natl. Acad. Sci. U. S. A.*, 102, 13521–13525, 2005.

659 Haverd, V., Smith, B., Nieradzik, L. P., and Briggs, P. R.: A stand-alone tree demography and landscape structure module for
660 Earth system models: integration with inventory data from temperate and boreal forests, *Biogeosciences*, 11, 4039–4055, 2014.

661 Hayes, D. J., Turner, D. P., Stinson, G., McGuire, A. D., Wei, Y., West, T. O., Heath, L. S., Jong, B., McConkey, B. G.,
662 Birdsey, R. A., Kurz, W. A., Jacobson, A. R., Huntzinger, D. N., Pan, Y., Post, W. M., and Cook, R. B.: Reconciling estimates

663 of the contemporary North American carbon balance among terrestrial biosphere models, atmospheric inversions, and a new
664 approach for estimating net ecosystem exchange from inventory-based data, *Glob. Chang. Biol.*, 18, 1282–1299, 2012.

665 Hember, R. A., Kurz, W. A., Metsaranta, J. M., Black, T. A., Guy, R. D., and Coops, N. C.: Accelerating regrowth of temperate-
666 maritime forests due to environmental change, *Glob. Chang. Biol.*, 18, 2026–2040, 2012.

667 Hermosilla, T., Wulder, M. A., White, J. C., Coops, N. C., and Hobart, G. W.: An integrated Landsat time series protocol for
668 change detection and generation of annual gap-free surface reflectance composites, *Remote Sens. Environ.*, 158, 220–234,
669 2015a.

670 Hermosilla, T., Wulder, M. A., White, J. C., Coops, N. C., and Hobart, G. W.: Regional detection, characterization, and
671 attribution of annual forest change from 1984 to 2012 using Landsat-derived time-series metrics, *Remote Sens. Environ.*, 170,
672 121–132, 2015b.

673 Hermosilla, T., Wulder, M. A., White, J. C., Coops, N. C., Hobart, G. W., and Campbell, L. B.: Mass data processing of time
674 series Landsat imagery: pixels to data products for forest monitoring, *International Journal of Digital Earth*, 9, 1035–1054,
675 2016.

676 Hermosilla, T., Wulder, M. A., White, J. C., Coops, N. C., and Hobart, G. W.: Disturbance-Informed Annual Land Cover
677 Classification Maps of Canada’s Forested Ecosystems for a 29-Year Landsat Time Series, *Can. J. Remote Sens.*, 44, 67–87,
678 2018.

679 Hermosilla, T., Wulder, M. A., White, J. C., and Coops, N. C.: Prevalence of multiple forest disturbances and impact on
680 vegetation regrowth from interannual Landsat time series (1985–2015), *Remote Sens. Environ.*, 233, 111403, 2019.

681 Hijmans, R. J., Van Etten, J., Cheng, J., Mattiuzzi, M., Sumner, M., Greenberg, J. A., Lamigueiro, O. P., Bevan, A., Racine,
682 E. B., Shortridge, A., and Others: Package “raster,” R package, 734, 2015.

683 Hirano, T., Suzuki, K., and Hirata, R.: Energy balance and evapotranspiration changes in a larch forest caused by severe
684 disturbance during an early secondary succession, *Agric. For. Meteorol.*, 232, 457–468, 2017.

685 Ju, J. and Masek, J. G.: The vegetation greenness trend in Canada and US Alaska from 1984–2012 Landsat data, *Remote Sens.*
686 *Environ.*, 176, 1–16, 2016.

687 Ju, W. and Chen, J. M.: Simulating the effects of past changes in climate, atmospheric composition, and fire disturbance on
688 soil carbon in Canada’s forests and wetlands, *Global Biogeochem. Cycles*, 22, <https://doi.org/10.1029/2007GB002935>, 2008.

689 Keenan, T. F. and Williams, C. A.: The Terrestrial Carbon Sink, *Annu. Rev. Environ. Resour.*, 43, 219–243, 2018.

690 Kim: Global soil wetness project phase 3 atmospheric boundary conditions (Experiment 1), Data Integration and Analysis
691 System (DIAS), Data set, 2017.

692 Körner, C.: Plant CO₂ responses: an issue of definition, time and resource supply, *New Phytol.*, 172, 393–411, 2006.

693 Kucharik, C. J., Foley, J. A., Delire, C., Fisher, V. A., Coe, M. T., Lenters, J. D., Young-Molling, C., Ramankutty, N., Norman,
694 J. M., and Gower, S. T.: Testing the performance of a dynamic global ecosystem model: Water balance, carbon balance, and
695 vegetation structure, *Global Biogeochem. Cycles*, 14, 795–825, 2000.

696 Kurz, W. A. and Apps, M. J.: Contribution of Northern Forests to the Global C Cycle: Canada as a Case Study, in: *Terrestrial*
697 *Biospheric Carbon Fluxes Quantification of Sinks and Sources of CO₂*, edited by: Wisniewski, J. and Sampson, R. N., Springer
698 Netherlands, Dordrecht, 163–176, 1993.

699 Kurz, W. A. and Apps, M. J.: A 70-year retrospective analysis of carbon fluxes in the Canadian forest sector, *Ecol. Appl.*, 9,
700 526–547, 1999.

701 Kurz, W. A., Apps, M. J., Beukema, S. J., and Lekstrum, T.: 20th century carbon budget of Canadian forests, *Tellus B Chem.*
702 *Phys. Meteorol.*, 47, 170–177, 1995.

703 Kurz, W. A., Beukema, S. J., and Apps, M. J.: Carbon budget implications of the transition from natural to managed disturbance
704 regimes in forest landscapes, *Mitigation and Adaptation Strategies for Global Change*, 2, 405–421, 1997.

705 Kurz, W. A., Stinson, G., Rampley, G. J., Dymond, C. C., and Neilson, E. T.: Risk of natural disturbances makes future
706 contribution of Canada’s forests to the global carbon cycle highly uncertain, *Proc. Natl. Acad. Sci. U. S. A.*, 105, 1551–1555,
707 2008.

708 Kurz, W. A., Dymond, C. C., White, T. M., Stinson, G., Shaw, C. H., Rampley, G. J., Smyth, C., Simpson, B. N., Neilson, E.
709 T., Trofymow, J. A., Metsaranta, J., and Apps, M. J.: CBM-CFS3: A model of carbon-dynamics in forestry and land-use
710 change implementing IPCC standards, *Ecol. Modell.*, 220, 480–504, 2009.

711 Kuuluvainen, T. and Gauthier, S.: Young and old forest in the boreal: critical stages of ecosystem dynamics and management
712 under global change, *Forest Ecosystems*, 5, 26, 2018.

713 Lange, S.: WFDE5 over land merged with ERA5 over the ocean (W5E5). V. 1.0. GFZ Data Services, 2019.

714 Lange, S.: ISIMIP3BASD (Version 2.3), <https://doi.org/10.5281/zenodo.3648654>, 2020a.

715 Lange, S.: The Inter-Sectoral Impact Model Intercomparison Project Input data set: GSWP3-W5E5, [https://www.](https://www.isimip.org/gettingstarted/input-data-bias-correction/details/80/)
716 [isimip.org/gettingstarted/input-data-bias-correction/details/80/](https://www.isimip.org/gettingstarted/input-data-bias-correction/details/80/), 2020b.

717 Latifovic, R., Pouliot, D., and Olthof, I.: Circa 2010 Land Cover of Canada: Local Optimization Methodology and Product
718 Development, *Remote Sensing*, 9, 1098, 2017.

719 Lenton, T. M., Held, H., Kriegler, E., Hall, J. W., Lucht, W., Rahmstorf, S., and Schellnhuber, H. J.: Tipping elements in the
720 Earth’s climate system, *Proc. Natl. Acad. Sci. U. S. A.*, 105, 1786–1793, 2008.

721 Le Quéré, C., Andrew, R. M., Friedlingstein, P., Sitch, S., Hauck, J., Pongratz, J., Pickers, P. A., Korsbakken, J. I., Peters, G.
722 P., Canadell, J. G., Arneeth, A., Arora, V. K., Barbero, L., Bastos, A., Bopp, L., Chevallier, F., Chini, L. P., Ciais, P., Doney,
723 S. C., Gkritzalis, T., Goll, D. S., Harris, I., Haverd, V., Hoffman, F. M., Hoppema, M., Houghton, R. A., Hurtt, G., Ilyina, T.,
724 Jain, A. K., Johannessen, T., Jones, C. D., Kato, E., Keeling, R. F., Goldewijk, K. K., Landschützer, P., Lefèvre, N., Lienert,
725 S., Liu, Z., Lombardozi, D., Metzl, N., Munro, D. R., Nabel, J. E. M. S., Nakaoka, S.-I., Neill, C., Olsen, A., Ono, T., Patra,
726 P., Peregon, A., Peters, W., Peylin, P., Pfeil, B., Pierrot, D., Poulter, B., Rehder, G., Resplandy, L., Robertson, E., Rocher, M.,
727 Rödenbeck, C., Schuster, U., Schwinger, J., Séférian, R., Skjelvan, I., Steinhoff, T., Sutton, A., Tans, P. P., Tian, H., Tilbrook,
728 B., Tubiello, F. N., van der Laan-Luijkx, I. T., van der Werf, G. R., Viovy, N., Walker, A. P., Wiltshire, A. J., Wright, R.,
729 Zaehle, S., and Zheng, B.: Global carbon budget 2018, *Earth Syst. Sci. Data*, 10, 2141–2194, 2018.

730 Li, R. and Arora, V. K.: Effect of mosaic representation of vegetation in land surface schemes on simulated energy and carbon
731 balances, *Biogeosciences*, 9, 593–605, 2012.

732 Liu, H.: Changes in the surface energy budget after fire in boreal ecosystems of interior Alaska: An annual perspective, *J.*
733 *Geophys. Res.*, 110, <https://doi.org/10.1029/2004jd005158>, 2005.

734 Luyssaert, S., Jammot, M., Stoy, P. C., Estel, S., Pongratz, J., Ceschia, E., Churkina, G., Don, A., Erb, K., Ferlicoq, M., Gielen,
735 B., Grünwald, T., Houghton, R. A., Klumpp, K., Knohl, A., Kolb, T., Kummerle, T., Laurila, T., Lohila, A., Loustau, D.,
736 McGrath, M. J., Meyfroidt, P., Moors, E. J., Naudts, K., Novick, K., Otto, J., Pilegaard, K., Pio, C. A., Rambal, S., Rebmann,
737 C., Ryder, J., Suyker, A. E., Varlagin, A., Wattenbach, M., and Dolman, A. J.: Land management and land-cover change have
738 impacts of similar magnitude on surface temperature, *Nat. Clim. Chang.*, 4, 389–393, 2014.

739 MacKay, M. D., Meyer, G., and Melton, J. R.: On the Discretization of Richards Equation in Canadian Land Surface Models,
740 *Atmosphere-Ocean*, 1–11, 2022.

741 MacKenzie, W. H. and Meidinger, D. V.: The Biogeoclimatic Ecosystem Classification Approach: an ecological framework
742 for vegetation classification, *Phytocoenologia*, 48, 203–213, 2018.

743 Maltman, J. C., Hermosilla, T., Wulder, M. A., Coops, N. C., and White, J. C.: Estimating and mapping forest age across
744 Canada’s forested ecosystems, *Remote Sens. Environ.*, 290, 113529, 2023.

745 Maness, H., Kushner, P. J., and Fung, I.: Summertime climate response to mountain pine beetle disturbance in British
746 Columbia, *Nat. Geosci.*, 6, 65–70, 2012.

747 Marchand, Girardin, and Gauthier: Untangling methodological and scale considerations in growth and productivity trend
748 estimates of Canada’s forests, *Environ. Toxicol. Water Qual.*, <https://doi.org/10.1088/1748-9326/aad82a/meta>, 2018.

749 Ma, Z., Peng, C., Zhu, Q., Chen, H., Yu, G., Li, W., Zhou, X., Wang, W., and Zhang, W.: Regional drought-induced reduction
750 in the biomass carbon sink of Canada’s boreal forests, *Proc. Natl. Acad. Sci. U. S. A.*, 109, 2423–2427, 2012.

751 Melton, J. R. and Arora, V. K.: Sub-grid scale representation of vegetation in global land surface schemes: implications for
752 estimation of the terrestrial carbon sink, *Biogeosciences*, 11, 1021–1036, 2014.

753 Melton, J. R. and Arora, V. K.: Competition between plant functional types in the Canadian Terrestrial Ecosystem Model
754 (CTEM) v. 2.0, *Geosci. Model Dev.*, 9, 323–361, 2016.

755 Melton, J. R., Sospedra-Alfonso, R., and McCusker, K. E.: Tiling soil textures for terrestrial ecosystem modelling via
756 clustering analysis: a case study with CLASS-CTEM (version 2.1), *Geoscientific Model Development*, 10, 2761–2783, 2017.

757 Melton, J. R., Arora, V. K., Wisernig-Cojoc, E., Seiler, C., Fortier, M., Chan, E., and Teckentrup, L.: CLASSIC v1. 0: the
758 open-source community successor to the Canadian Land Surface Scheme (CLASS) and the Canadian Terrestrial Ecosystem
759 Model (CTEM)–Part 1: Model framework and site-level performance, *Geoscientific Model Development*, 13, 2825–2850,
760 2020.

761 Meyer, G., Humphreys, E. R., Melton, J. R., Cannon, A. J., and Lafleur, P. M.: Simulating shrubs and their energy and carbon
762 dioxide fluxes in Canada’s Low Arctic with the Canadian Land Surface Scheme Including Biogeochemical Cycles
763 (CLASSIC), *Biogeosciences*, 18, 3263–3283, 2021.

764 Moorcroft, P. R., Hurtt, G. C., and Pacala, S. W.: A METHOD FOR SCALING VEGETATION DYNAMICS: THE
765 ECOSYSTEM DEMOGRAPHY MODEL (ED), *Ecol. Monogr.*, 71, 557–586, 2001.

766 Nabel, J. E. M. S., Naudts, K., and Pongratz, J.: Accounting for forest age in the tile-based dynamic global vegetation model
767 JSBACH4 (4.20p7; git feature/forests) – a land surface model for the ICON-ESM, *Geosci. Model Dev.*, 13, 185–200, 2020.

768 Naudts, K., Ryder, J., McGrath, M. J., Otto, J., Chen, Y., Valade, A., Bellasen, V., Berhongaray, G., Bönisch, G., Campioli,
769 M., Ghattas, J., De Groote, T., Haverd, V., Kattge, J., MacBean, N., Maignan, F., Merilä, P., Penuelas, J., Peylin, P., Pinty, B.,
770 Pretzsch, H., Schulze, E. D., Solyga, D., Vuichard, N., Yan, Y., and Luysaert, S.: A vertically discretised canopy description
771 for ORCHIDEE (SVN r2290) and the modifications to the energy, water and carbon fluxes, *Geosci. Model Dev.*, 8, 2035–
772 2065, 2015.

773 Nocedal, J. and Wright, S.J. eds., *Numerical optimization*. New York, NY: Springer New York. 1999.

774 Pan, Y., Chen, J. M., Birdsey, R., McCullough, K., He, L., and Deng, F.: Age structure and disturbance legacy of North
775 American forests, *Biogeosci. Discuss.*, 7, 979–1020, 2010.

776 Pan, Y., Birdsey, R. A., Phillips, O. L., and Jackson, R. B.: The Structure, Distribution, and Biomass of the World’s Forests,
777 *Annu. Rev. Ecol. Evol. Syst.*, 44, 593–622, 2013.

778 Peng, Y., Arora, V. K., Kurz, W. A., Hember, R. A., Hawkins, B. J., Fyfe, J. C., and Werner, A. T.: Climate and atmospheric
779 drivers of historical terrestrial carbon uptake in the province of British Columbia, Canada, *Biogeosciences*, 11, 635–649, 2014.

780 Pongratz, J., Dolman, H., Don, A., Erb, K.-H., Fuchs, R., Herold, M., Jones, C., Kuemmerle, T., Luysaert, S., Meyfroidt, P.,
781 and Naudts, K.: Models meet data: Challenges and opportunities in implementing land management in Earth system models,
782 *Glob. Chang. Biol.*, 24, 1470–1487, 2018.

783 Potapov, P., Hansen, M. C., Stehman, S. V., Loveland, T. R., and Pittman, K.: Combining MODIS and Landsat imagery to
784 estimate and map boreal forest cover loss, *Remote Sens. Environ.*, 112, 3708–3719, 2008.

785 Puettmann, K. J., Wilson, S. M., Baker, S. C., Donoso, P. J., Drössler, L., Amente, G., Harvey, B. D., Knoke, T., Lu, Y.,
786 Nocentini, S., Putz, F. E., Yoshida, T., and Bauhus, J.: Silvicultural alternatives to conventional even-aged forest management
787 - what limits global adoption?, *Forest Ecosystems*, 2, 1–16, 2015.

788 R core team: *R: A language and environment for statistical computing*, 2013.

789 Reich, P. B., Sendall, K. M., Stefanski, A., Rich, R. L., Hobbie, S. E., and Montgomery, R. A.: Effects of climate warming on
790 photosynthesis in boreal tree species depend on soil moisture, *Nature*, 562, 263–267, 2018.

791 Salkfield, Walton, and Mackenzie: *Biogeoclimatic ecosystem classification map*, Ministry of Forests, Lands, Natural
792 Resource, 2016.

793 Seiler, C., Melton, J. R., Arora, V. K., and Wang, L.: CLASSIC v1. 0: the open-source community successor to the Canadian
794 Land Surface Scheme (CLASS) and the Canadian Terrestrial Ecosystem Model (CTEM)--Part 2: Global benchmarking,
795 *Geoscientific Model Development*, 14, 2371–2417, 2021.

796 Shangguan, W., Hengl, T., Mendes de Jesus, J., Yuan, H., and Dai, Y.: Mapping the global depth to bedrock for land surface
797 modeling, *J. Adv. Model. Earth Syst.*, 9, 65–88, 2017.

798 Shevliakova, E., Pacala, S. W., Malyshev, S., Hurtt, G. C., Milly, P. C. D., Caspersen, J. P., Sentman, L. T., Fisk, J. P., Wirth,
799 C., and Crevoisier, C.: Carbon cycling under 300 years of land use change: Importance of the secondary vegetation sink,
800 *Global Biogeochem. Cycles*, 23, <https://doi.org/10.1029/2007gb003176>, 2009.

801 Shrestha, B. M. and Chen, H. Y. H.: Effects of stand age, wildfire and clearcut harvesting on forest floor in boreal mixedwood
802 forests, *Plant Soil*, 336, 267–277, 2010.

803 Shrestha, R. K., Arora, V. K., and Melton, J. R.: The sensitivity of simulated competition between different plant functional
804 types to subgrid-scale representation of vegetation in a land surface model, *J. Geophys. Res. Biogeosci.*, 121, 809–828, 2016.

805 Skakun, R., Whitman, E., Little, J. M., and Parisien, M.-A.: Area burned adjustments to historical wildland fires in Canada,
806 *Environ. Res. Lett.*, 16, 064014, 2021.

807 Stinson, G., Kurz, W. A., Smyth, C. E., Neilson, E. T., Dymond, C. C., Metsaranta, J. M., Boisvenue, C., Rampley, G. J., Li,
808 Q., White, T. M., and Others: An inventory-based analysis of Canada’s managed forest carbon dynamics, 1990 to 2008, *Glob.
809 Chang. Biol.*, 17, 2227–2244, 2011.

810 Stinson, G., Thandi, G., Aitkin, D., Bailey, C., Boyd, J., Colley, M., Fraser, C., Gelhorn, L., Groenewegen, K., Hogg, A.,
811 Kapron, J., Leboeuf, A., Makar, M., Montigny, M., Pittman, B., Price, K., Salkeld, T., Smith, L., Viveiros, A., and Wilson, D.:
812 A new approach for mapping forest management areas in Canada, *For. Chron.*, 95, 101–112, 2019.

813 Stocker, B. D., Spahni, R., and Joos, F.: DYP TOP: a cost-efficient TOPMODEL implementation to simulate sub-grid spatio-
814 temporal dynamics of global wetlands and peatlands, *Geosci. Model Dev. Discuss.*, 7, 4875–4930, 2014.

815 Sulla-Menashe, D., Woodcock, C. E., and Friedl, M. A.: Canadian boreal forest greening and browning trends: an analysis of
816 biogeographic patterns and the relative roles of disturbance versus climate drivers, *Environ. Res. Lett.*, 13, 014007, 2018.

817 Swart, N. C., Cole, J. N. S., Kharin, V. V., Lazare, M., Scinocca, J. F., Gillett, N. P., Anstey, J., Arora, V., Christian, J. R.,
818 Hanna, S., Jiao, Y., Lee, W. G., Majaess, F., Saenko, O. A., Seiler, C., Seinen, C., Shao, A., Sigmond, M., Solheim, L., von
819 Salzen, K., Yang, D., and Winter, B.: The Canadian Earth System Model version 5 (CanESM5.0.3), *Geosci. Model Dev.*, 12,
820 4823–4873, 2019.

821 Torres-Rojas, L., Vergopolan, N., Herman, J.D. and Chaney, N.W., 2022. Towards an Optimal Representation of Sub-Grid
822 Heterogeneity in Land Surface Models. *Water Resources Research*, 58(12), p.e2022WR032233.

823 Van Wagner, C. E.: The historical pattern of annual burned area in Canada, *For. Chron.*, 64, 182–185, 1988.

824 Versegny, D.: CLASS--The Canadian land surface scheme (v. 3.6. 2), Climate Research Division, Science and Technology
825 Branch, Environment Canada, 35, 2017.

826 Versegny, D. L.: The Canadian land surface scheme (CLASS): Its history and future, *Atmosphere-Ocean*, 38, 1–13, 2000.

827 Versegny, D. L.: Class-A Canadian land surface scheme for GCMS. I. Soil model, *Int. J. Climatol.*, 11, 111–133, 2007.

828 Versegny, D. L., McFarlane, N. A., and Lazare, M.: Class—A Canadian land surface scheme for GCMS, II. Vegetation model
829 and coupled runs, *Int. J. Climatol.*, 13, 347–370, 1993.

830 Wang, L., Bartlett, P., Arora, V. K., Chan, E., and Curasi, S. R.: Mapping of ESA CCI land cover data to plant functional types
831 for use in the CLASSIC land model, *EGUsphere*, <https://doi.org/10.5194/egusphere-2022-923>, 2022.

832 Weber, M. G. and Flannigan, M. D.: Canadian boreal forest ecosystem structure and function in a changing climate: impact
833 on fire regimes, *Environ. Rev.*, 5, 145–166, 1997.

834 White, J. C., Wulder, M. A., Hermosilla, T., Coops, N. C., and Hobart, G. W.: A nationwide annual characterization of 25
835 years of forest disturbance and recovery for Canada using Landsat time series, *Remote Sens. Environ.*, 194, 303–321, 2017.

836 World Resources Institute: Canada’s Forests at a Crossroads: An Assessment in the Year 2000 : a Global Forest Watch Canada
837 Report, World Resources Institute, 114 pp., 2000.

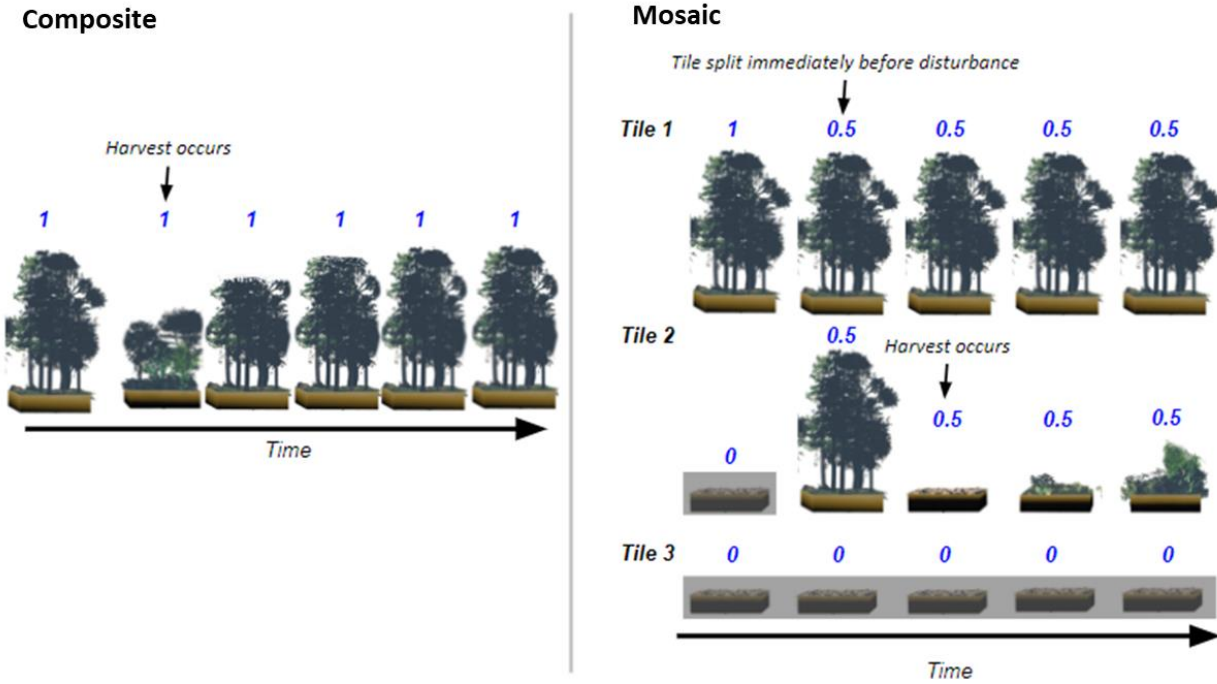
838 Wulder, M. A., Hermosilla, T., White, J. C., and Coops, N. C.: Biomass status and dynamics over Canada’s forests:
839 Disentangling disturbed area from associated aboveground biomass consequences, *Environ. Res. Lett.*, 15, 094093, 2020.

840 Yang, X., Richardson, T. K., and Jain, A. K.: Contributions of secondary forest and nitrogen dynamics to terrestrial carbon
841 uptake, *Biogeosciences*, 7, 3041–3050, 2010.

842 Yue, C., Ciais, P., Luyssaert, S., Li, W., McGrath, M. J., Chang, J., and Peng, S.: Representing anthropogenic gross land use
843 change, wood harvest, and forest age dynamics in a global vegetation model ORCHIDEE-MICT v8.4.2, *Geosci. Model Dev.*,
844 11, 409–428, 2018a.

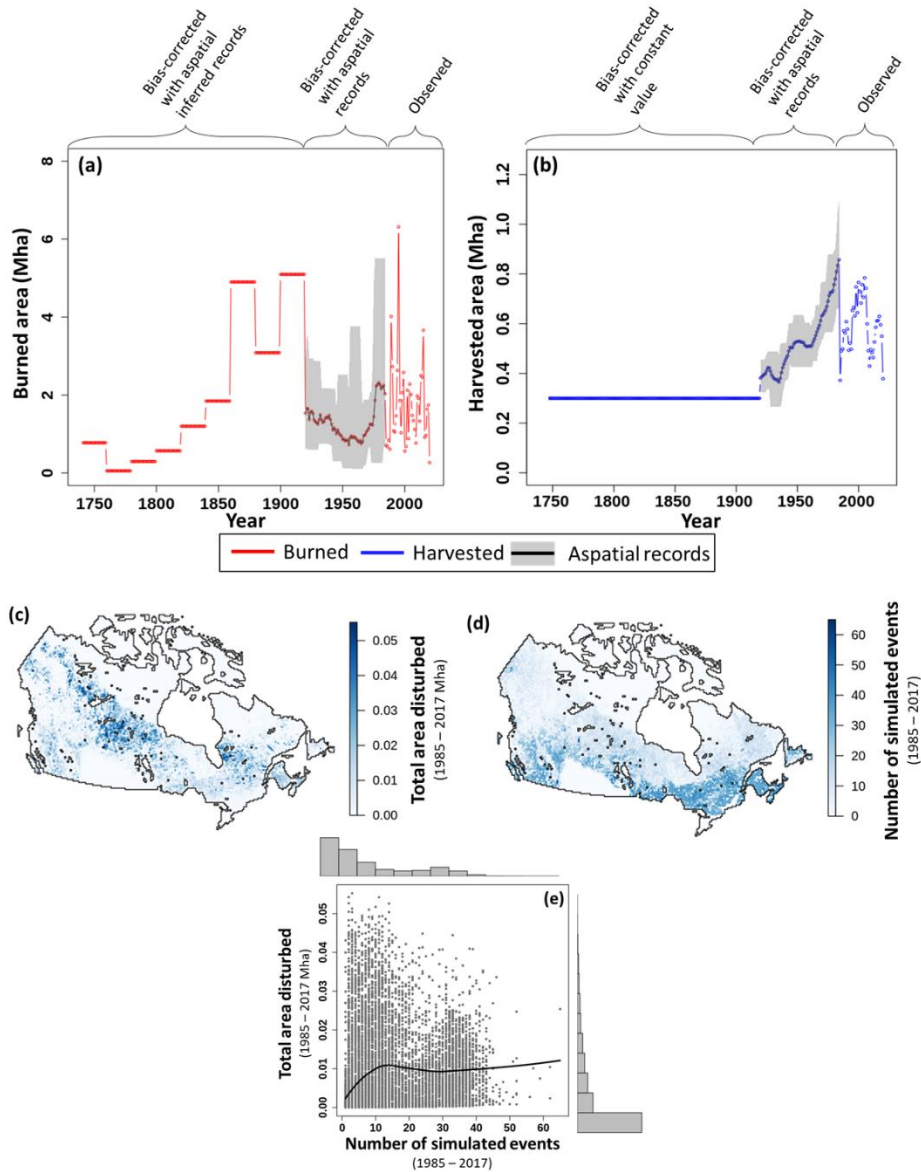
845 Yue, C., Ciais, P., and Li, W.: Smaller global and regional carbon emissions from gross land use change when considering
846 sub-grid secondary land cohorts in a global dynamic vegetation model, *Biogeosciences*, 15, 1185–1201, 2018b.

847 Zaehle, S., Sitch, S., Prentice, I. C., Liski, J., Cramer, W., Erhard, M., Hickler, T., and Smith, B.: The importance of age-
848 related decline in forest NPP for modeling regional carbon balances, *Ecol. Appl.*, 16, 1555–1574, 2006.



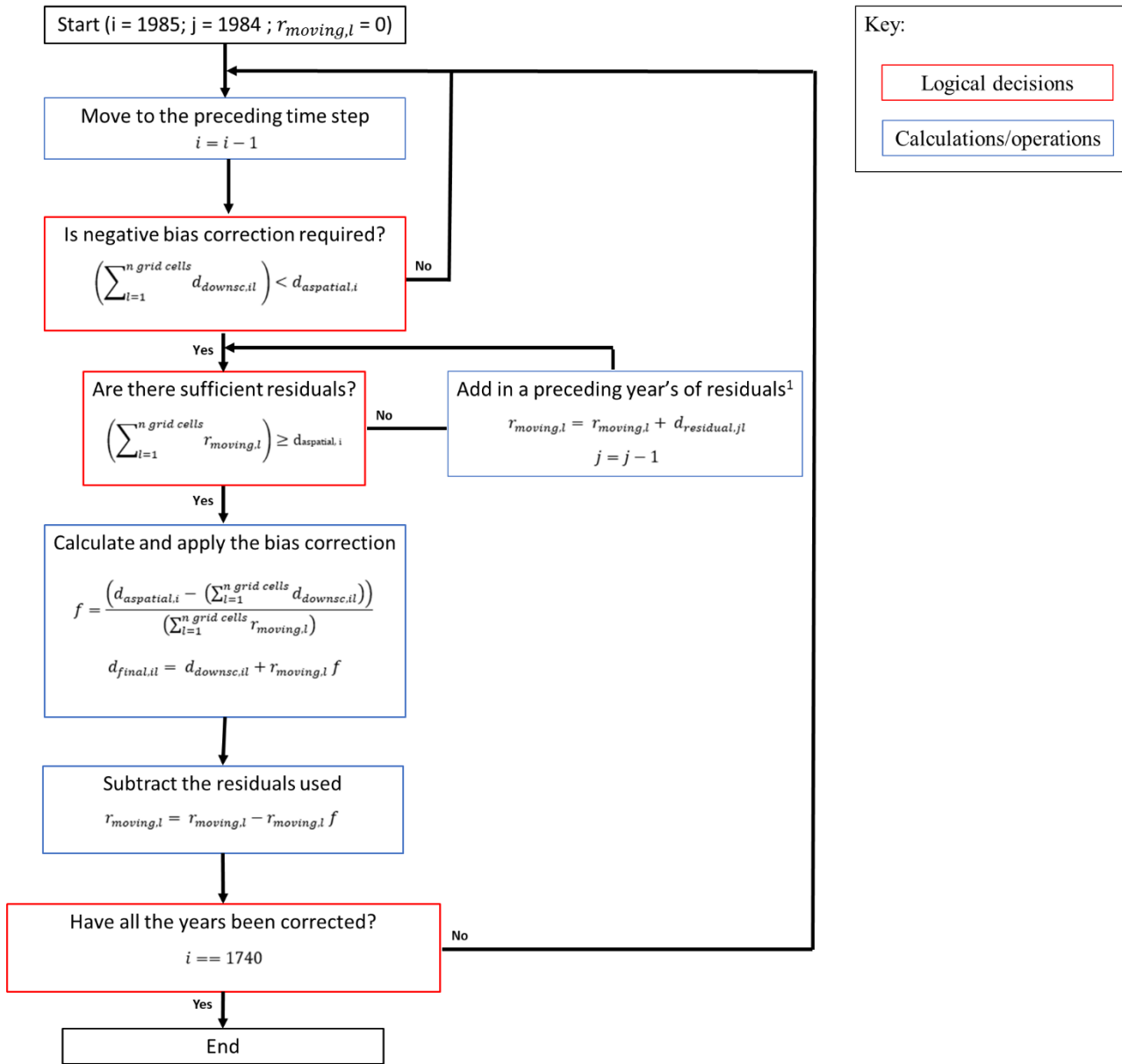
850

851 **Figure 1: Illustrative diagram contrasting the composite (1-tile) and mosaic (>1 tile) representations of disturbance implemented**
 852 **herein assuming a hypothetical scenario where 50% of a grid cell undergoes timber harvest. The fraction of a grid cell that is**
 853 **occupied by a tile is denoted above each tile. Tiles that are not active have a gray background (e.g. Tile 3 across all time steps).**



854

855 **Figure 2:** Plots of the disturbance drivers over time. a) annual total burned and b) harvested area from 1740 - 2020. Observed
 856 indicates the period that uses the Landsat fire and harvest observations (Hermosilla et al., 2016, 2015a, b). Bias-corrected with
 857 aspatial records indicates the period where the disturbance was inferred from 2019 stand age (Maltman et al., 2023) and bias-
 858 corrected using aspatial harvested and burned area (Skakun et al., 2021; World Resources Institute, 2000; Van Wagner, 1988). Bias-
 859 corrected with aspatial inferred records and bias-corrected with constant value indicate the period where the inferred disturbance
 860 was bias-corrected based on Kurz et al., (1995) and Chen et al., (2000) respectively. The aspatial records line is the nine-year running
 861 mean, min., and max. of the aspatial total harvested and burned area data sets. c) Per-grid cell total area disturbed (1985 - 2017)
 862 and d) the total number of simulated events (1985 - 2017). e) Per-grid cell total area disturbed, excluding un-disturbed cells, plotted
 863 against the total number of simulated events. The black line is a LOESS curve. Note that a simulated event combines all the individual
 864 fire or harvest events that occur in a grid cell in a single year, with a maximum of two simulated events per year (one fire and one
 865 harvest) occurring in each grid cell.



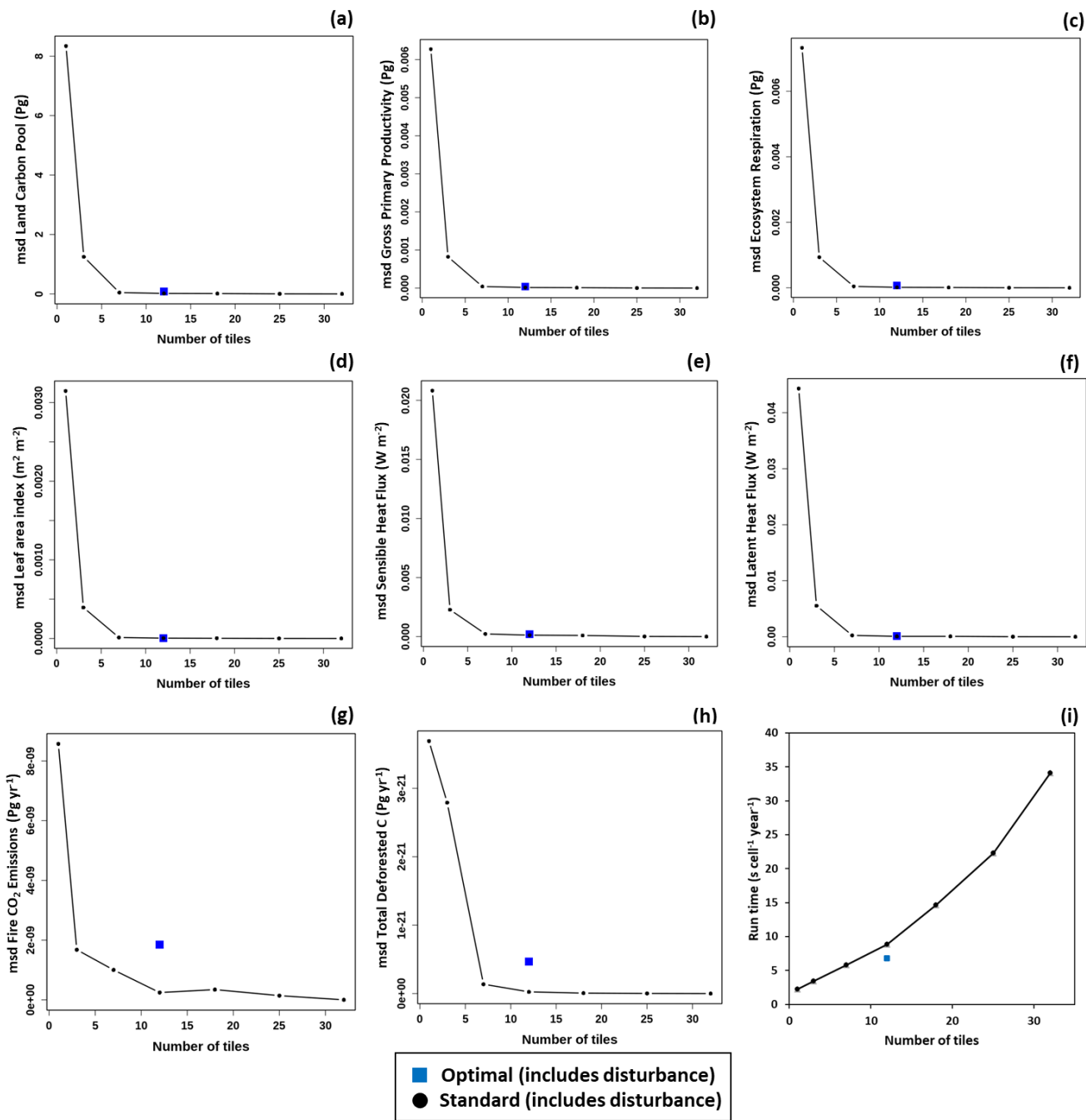
866

867

868

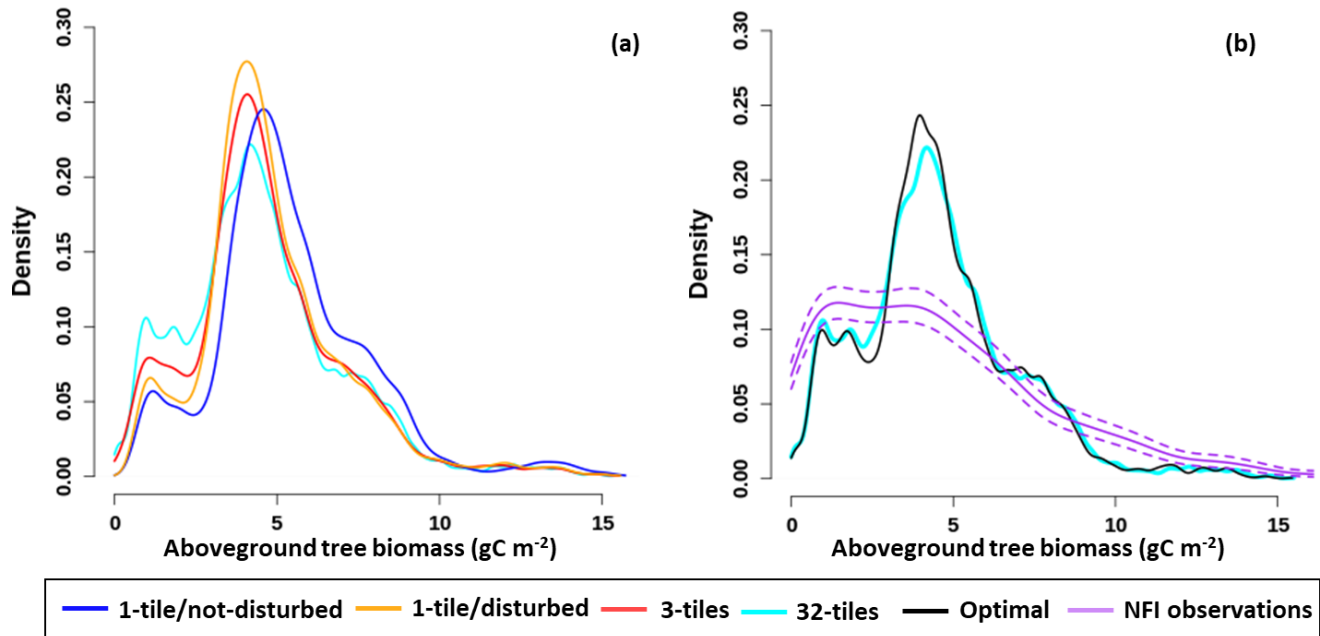
869

Figure 3: A schematic diagram of the negative bias correction algorithm with applicable equations and logical tests. ¹Not shown: When the spatially explicit residuals are exhausted they are replenished using the entire remotely sensed and stand age inferred disturbance record.



870

871 **Figure 4: Plots of the mean squared deviation (msd; 1985 – 2017; Eqn 11) for a) the land carbon pool (cLand), b) gross primary**
 872 **productivity (GPP), c) ecosystem respiration (ER), d) leaf area index (LAI), e) sensible heat flux (HFSS), f) latent heat flux (HFSS),**
 873 **g) fire emissions (fFire), and h) total deforested carbon (fDeforestTotal) for model runs including disturbance with varying numbers**
 874 **of tiles (1 – 32) compared against the run including disturbance with the largest number of tiles (32). i) The run time for each**
 875 **configuration. Values are also shown for the optimal model run including disturbance with 12 tiles (tile preservation parameter [tpp]**
 876 **= 4; and relative height threshold [rht] = 0.16).**



877

878

879

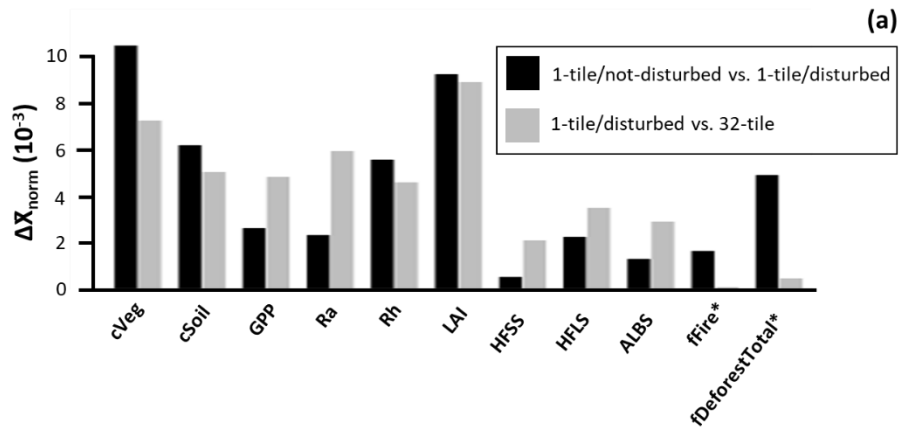
880

881

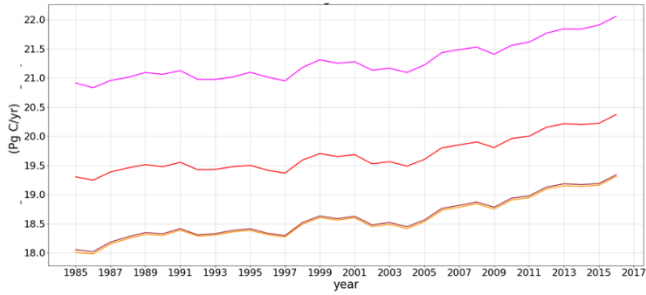
882

883

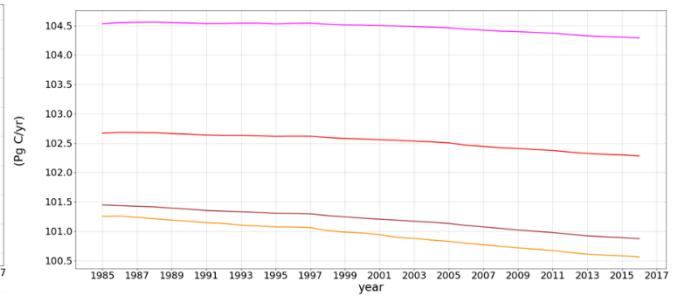
Figure 5: Weighted histogram of aboveground tree biomass for forested areas of Canada at the end of a) a selection of model runs including the 1-tile/not-disturbed run, 1-tile/disturbed, 3-tiles, and 32-tiles. As well as for b) 32-tile, optimal (12 tiles, 4 preserved tiles, and a threshold of 0.16), and observations from the National Forest Inventory (NFI) (Gillis et al., 2005). All runs using >1 tile include disturbance. The bootstrapped 95% CI for the NFI observations is also shown. The contributions of all forested subgrid areas weighted by their fractional area within the modeled region are considered. An area is classified as forested if it contains at least 50% tree cover.



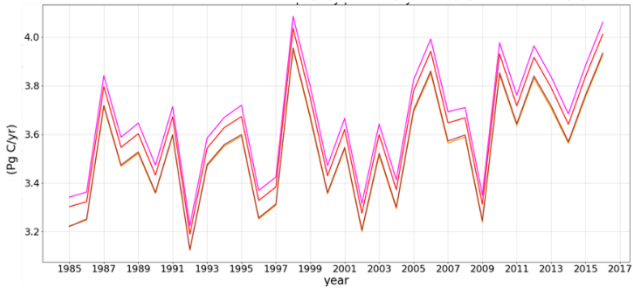
(b) Vegetation carbon (cVeg)



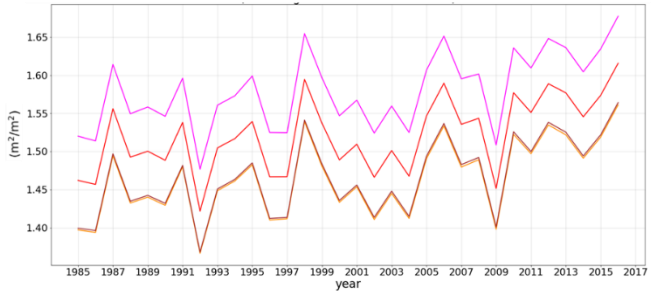
(c) Soil carbon (cSoil)

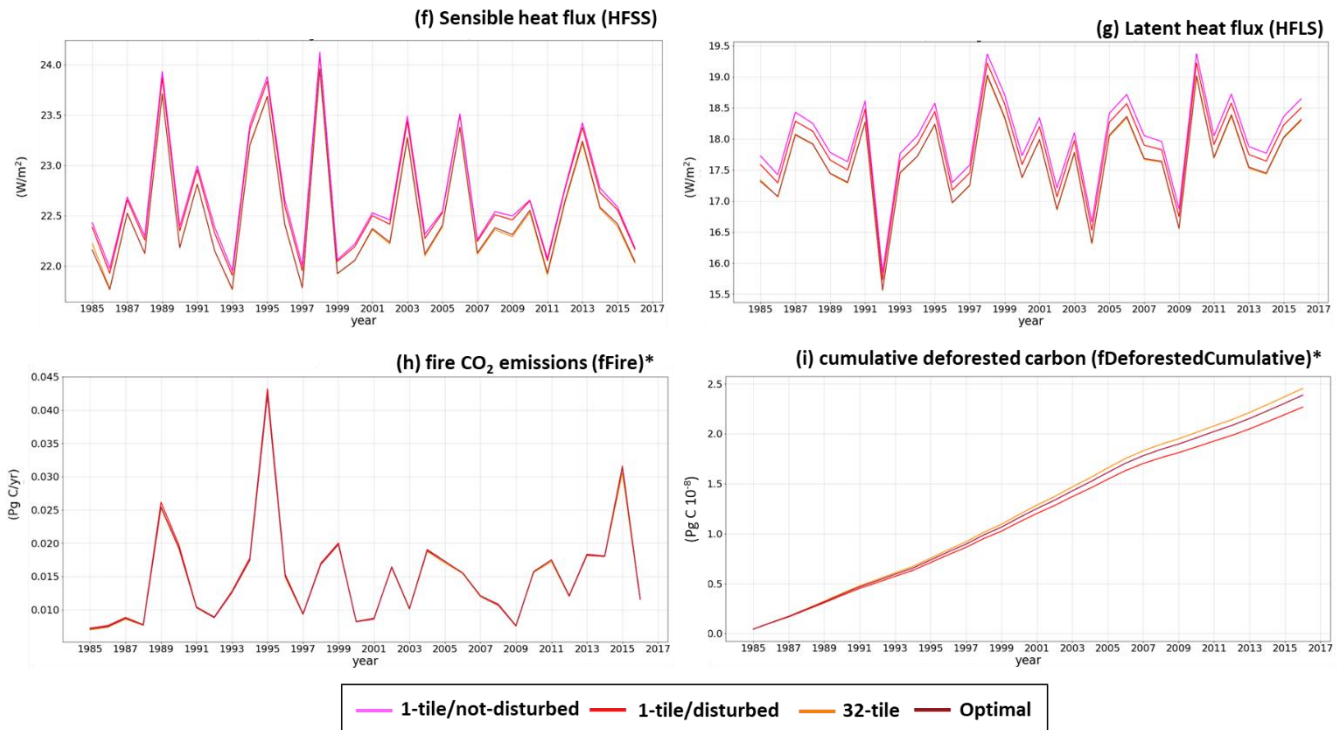


(d) Gross primary productivity (GPP)



(e) Leaf area index (LAI)





885

886 **Figure 6:** a) Plot of the normalized response metric ($\Delta\bar{X}_{norm}$; Eqn 12) for the 1-tile/not-disturbed versus 1-tile/disturbed and 1-tile/disturbed versus 32-tile for vegetation carbon (cVeg), soil carbon (cSoil), gross primary productivity (GPP), autotrophic respiration (Ra), heterotrophic respiration (Rh), leaf area index (LAI), sensible heat flux (HFSS), latent heat flux (HFLS), albedo (ALBS), fire emissions (fFire), and total deforested carbon (fDeforestTotal). Time series plots of b) cVeg, c) cSoil, d) GPP, e) LAI f) HFSS, g) HFLS, h) fFire, and i) cumulative deforested carbon (fDeforestedCumulative; the running sum of fDeforestTotal starting in 1985) for 1-tile/not-disturbed, the 1-tile/disturbed, 32-tile and optimal ($tpp = 4$; $rht = 0.16$; purple). All runs using >1 tile include disturbance. In the “a” panel a normalized response of zero indicates that there are no differences between the runs. *denotes disturbance-related fluxes that are omitted in the 1-tile/not-disturbed model run.

894 **Tables**

895 **Table 1:** The PFT-specific fire emission fractions (υ) used to calculate C emissions to the atmosphere due to fire for each live
 896 vegetation component (i.e. both structural and non-structural leaves, stems, and roots) and the litter pool. As well as the PFT-specific
 897 mortality fractions (Θ) used to calculate the quantity of C from each live vegetation component transferred to the litter pool. Crop
 898 PFTs are not impacted by fire and therefore not assigned fractions (Melton and Arora, 2016).

PFT type	green leaves		brown leaves		stems		roots		litter
	combusted (υ_L)	litter (Θ_L)	combusted (υ_B)	litter (Θ_B)	combusted (υ_S)	litter (Θ_S)	combusted (υ_R)	litter (Θ_R)	combusted (υ_D)
Tree	0.42	0.20	-	-	0.12	0.60	0.00	0.10	0.30
Herbaceous	0.48	0.10	0.54	0.06	0.00	0.00	0.00	0.25	0.42
Shrub	0.42	0.20	-	-	0.12	0.60	0.00	0.10	0.36

899

900

901 **Table 2: The fraction of harvest-affected biomass transferred to different wood product pools for herbaceous PFTs and woody PFTs**
 902 **(ϵ). The fractions for woody PFTs differ depending on aboveground biomass density (Arora and Boer, 2010).**

	Aboveground biomass density (kgC m ⁻²)	Fraction of deforested biomass emitted to the atmosphere (ϵ_A)	Fraction of deforested biomass as slash/pulp and paper products (ϵ_D)	Fraction of deforested biomass as durable wood products (ϵ_S)
Woody PFTs	> 4.0	0.15	0.70	0.15
	1.0 - 4.0	0.30	0.70	0.00
	< 1.0	0.45	0.55	0.00
Herbaceous PFTs	NA	0.45	0.55	0.00

903
 904 **Table 3: An overview of the simulations conducted in this study.**

Abbreviation	Land surface representation	Includes disturbance	Max available tiles	Relative height threshold	Tile preservation parameter
1-tile/not-disturbed	composite	No	1	-	-
1-tile/disturbed	composite	Yes	1	-	-
3-tile	mosaic	Yes	3	-	-
7-tiles	mosaic	Yes	7	-	-
12-tile	mosaic	Yes	12	-	-
18-tile	mosaic	Yes	18	-	-
25-tile	mosaic	Yes	25	-	-
32-tile	mosaic	Yes	32	-	-
Optimized	mosaic	Yes	12	0.04	4
-	mosaic	Yes	12	0.08	4
-	mosaic	Yes	12	0.16	4
-	mosaic	Yes	12	0.04	6
-	mosaic	Yes	12	0.08	6
-	mosaic	Yes	12	0.16	6